

# Faint LAEs near $z > 4.7$ C IV absorbers revealed by MUSE<sup>★</sup>

Díaz, C. G.<sup>1,2,3</sup> †, Ryan-Weber, E. V.<sup>4,5</sup>, Karman, W.<sup>6</sup>, Caputi, K. I.<sup>6</sup>,  
Salvadori, S.<sup>7,8</sup>, Crighton, N. H.<sup>4</sup>, Ouchi, M.<sup>9,10</sup>, and Vanzella, E.<sup>11</sup>

<sup>1</sup>*Gemini Observatory, Southern Operations Center, La Serena, Chile*

<sup>2</sup>*Instituto de Ciencias Astronómicas, de la Tierra y del Espacio (ICATE), San Juan, Argentina*

<sup>3</sup>*Consejo de Investigaciones Científicas y Técnicas (CONICET), San Juan, Argentina*

<sup>4</sup>*Centre for Astrophysics and Supercomputing, Swinburne University of Technology, Hawthorn, VIC, Australia*

<sup>5</sup>*ARC Centre of Excellence for All Sky Astrophysics in 3 Dimensions (ASTRO 3D)*

<sup>6</sup>*Kapteyn Astronomical Institute, University of Groningen, Groningen, The Netherlands*

<sup>7</sup>*Dipartimento di Fisica e Astronomia, Università di Firenze, via G. Sansone 1, Sesto Fiorentino, Italy*

<sup>8</sup>*Istituto Nazionale di Astrofisica (INAF) - Osservatorio Astrofisico di Arcetri, Largo E. Fermi 5, Firenze, Italy*

<sup>9</sup>*Institute for Cosmic Ray Research, The University of Tokyo, Kashiwa, Japan*

<sup>10</sup>*Kavli Institute for the Physics and Mathematics of the Universe (WPI), The University of Tokyo, Kashiwa, Japan*

<sup>11</sup>*INAF - Osservatorio di Astrofisica e Scienza dello Spazio di Bologna, via Piero Gobetti 93/3, I-40129 Bologna, Italy*

Accepted XXX. Received YYY; in original form ZZZ

## ABSTRACT

We present the results from the search for Lyman Alpha emitters (LAEs) in the proximity of 11 C IV absorption systems at  $z > 4.7$  in the spectrum of the QSO J1030+0524, using data from MUSE. We have found multiple LAE candidates close to four C IV systems at  $z_{\text{C IV}} = 4.94\text{--}5.74$  with  $\log_{10}(N_{\text{C IV}}[\text{cm}^{-2}]) > 13.5$ . At  $z = 5\text{--}6$ , C IV systems with  $W_0(\text{C IV}) > 0.2 \text{ \AA}$  seem more likely to have galaxies with Ly $\alpha$  emission within  $\rho < 200$  proper kpc (4/5 cases), than the C IV systems with  $W_0(\text{C IV}) < 0.2 \text{ \AA}$  (0/6 cases). The impact parameter of LAE-C IV systems with equivalent widths  $W_0(\text{C IV}) > 0.5 \text{ \AA}$  is in the range  $11 \lesssim \rho \lesssim 200$  proper kpc (pkpc). Furthermore, all candidates are in the luminosity range  $0.18\text{--}1.15 L_{\text{Ly}\alpha}^*(z = 5.7)$ , indicating that the environment of C IV systems within 200 pkpc is populated by the faint end of the Ly $\alpha$  luminosity function. We report a  $0.28 L_{\text{Ly}\alpha}^*$  galaxy at a separation of  $\rho = 11$  pkpc from a strong C IV absorption ( $\log_{10}(N_{\text{C IV}}[\text{cm}^{-2}]) = 14.52$ ) at  $z_{\text{C IV}} = 5.72419$ . The prevalence of sub- $L_{\text{Ly}\alpha}^*$  galaxies in the proximity of  $z > 4.9$  C IV systems suggest that the absorbing material is rather young, likely ejected in the recent past of the galaxies at these redshifts. The connection between faint LAEs and high-ionization absorption systems reported in this work, is potentially a consequence of the role of low mass galaxies in the early evolution of the circum-galactic and intergalactic media.

**Key words:** galaxies: evolution, distances and redshifts, high-redshift, (galaxies:) intergalactic medium, (galaxies:) quasars: absorption lines.

## 1 INTRODUCTION

About 10 percent of the baryon content of the Universe is accounted for by condensed visible matter in galaxies, groups and clusters. The remaining large majority of baryons exist in a gaseous state outside of galaxies (e.g. Persic & Salucci 1992; Shull et al. 2012), covering a large range of temperatures and densities, from the gas in the multi-phase circum-galactic medium (CGM) within a few virial radii, to the diffuse intergalactic medium (IGM) filling the vast space between galaxies (Ferrara et al. 2005; Prochaska et al. 2011; Tejos

et al. 2014; Peebles et al. 2014; Werk et al. 2014; Lehner et al. 2014; Wakker et al. 2015; Wotta et al. 2016).

In the current cosmological framework of galaxy formation, cold streams of baryons from the IGM flow into galaxies providing the raw material for star-formation (Kereš et al. 2005; Dekel et al. 2009; Borthakur et al. 2015; Nielsen et al. 2013). However, only a fraction of the inflowing gas can form stars because star formation itself, via supernova explosions and stellar winds, introduces large amounts of energy and momentum to the interstellar medium (ISM) by removing large quantities of gas from the inner regions of the galaxies resulting in galactic winds or outflows (Oppenheimer & Davé 2008; Hopkins et al. 2012; Muratov et al. 2015). This source of mechanical feedback contributes regulating star-formation and is required by hydrodynamical simulations and semi-analytic models

<sup>★</sup> Based on observations at VLT, ESO program 095.A-0714.

† E-mail: gdiaz@gemini.edu

to reproduce several observational results such as: the star formation rate (SFR) and galaxy stellar mass functions (Oppenheimer et al. 2010; Hopkins et al. 2014; Somerville & Davé 2015), the fraction of gas and galaxy metallicities (Davé et al. 2011), the luminosity functions in the rest-frame UV and optical (Fontanot et al. 2017), and even the observed properties of present-day ancient dwarf galaxies dwelling in the Local Group (Salvadori et al. 2015; Revaz & Jablonka 2018). Moreover, outflows can introduce metals in the CGM and the IGM (Oppenheimer et al. 2009; Cen & Chisari 2011; Pallottini et al. 2014), which are commonly observed as metal absorption line systems in the spectra of background light sources like high redshift quasars (QSOs).

Metal absorption systems provide a wealth of information about the absorbing gas, including velocity, covering fraction, metallicity, density, temperature and ionization state. In recent years, observations have revealed the presence of gas accretion (Rubin et al. 2012; Bowen et al. 2016; Ho et al. 2017) and outflows of gas from high redshift star-forming galaxies (Pettini et al. 2001; Steidel et al. 2010; Bradshaw et al. 2013; Karman et al. 2014; Rubin et al. 2014). Triply ionized carbon (C IV) has now been detected in intervening systems out to redshifts  $z \sim 6.5$  (Ryan-Weber et al. 2009; Bosman et al. 2017; Codoreanu et al. 2018; Meyer et al. 2019; Cooper et al. 2019). The presence of C IV has been reported in the CGM of Lyman Break Galaxies (LBGs) at  $z = 2 - 3$ , with  $\log_{10}(N_{\text{C IV}}[\text{cm}^{-2}]) > 14$  within  $\sim 90$  proper kpc (pkpc) from the closest galaxy (Steidel et al. 2010; Turner et al. 2014) and tend to be commonly detected in regions of galaxy overdensity (Adelberger et al. 2005). Low redshift studies of C IV absorbers find a close association with galaxies out to  $\sim 250$  pkpc (Chen et al. 2001; Stocke et al. 2013; Ford et al. 2014; Bordoloi et al. 2014). In a series of papers Burchett et al. (2013, 2015, 2016) conducted a search for faint galaxies associated with low redshift ( $z < 0.015$ ) C IV systems and explore the relationship between individual galaxies as well as their environments. They found that C IV was preferentially associated with  $M_{\star} > 10^{9.5} M_{\odot}$  galaxies in low density environments. Although these observations demonstrate a connection between galaxies, the CGM and the IGM, we are just starting to understand the relation between the physical conditions in the ISM and the conditions of the gas outside of galaxies.

Several studies based on cosmological hydrodynamical simulations have found that the evolution of low ionization metal absorptions, like O I and C II are relatively insensitive to the choice of galactic feedback, whereas high ionization species like C IV and Si IV are highly sensitive to the feedback prescription (Tescari et al. 2011; Keating et al. 2016; Rahmati et al. 2016; García et al. 2017b). This is particularly important at high redshift where metal systems are possible tracers of galaxies hiding below current detection limits (Becker et al. 2015a).

At the end of the epoch of hydrogen reionization ( $z \sim 6$ ) the ionizing ultra-violet background (UVB) is predicted to have large spatial fluctuation in intensity and spectral slope (e.g. Mesinger & Furlanetto 2009; Finlator et al. 2015, 2016). The non-uniform spatial distribution of the ionizing sources results in a mean free path of ionizing photons that varies with density. The inclusion of these UVB fluctuations in simulated data improves the match to the observed statistics of high ionization metal ions like C IV and Si IV at  $z > 5$  (Oppenheimer et al. 2009; Finlator et al. 2016). In this scenario, the UVB is enhanced in environments dominated by ionizing sources. Therefore, studying the connection between galaxies and high ionization metal absorptions like C IV at  $z > 5$  can give us critical information about the production of metals and ionizing photons in such environments.

In three previous publications we have reported on the search for galaxies with the hydrogen Lyman- $\alpha$  line in emission (“Lyman Alpha Emitters” or LAEs) to characterize the environment of C IV systems at  $z \sim 5.7$ . The field of the QSO J1030+0524 was chosen because it contains 11 C IV absorption systems between  $4.7 < z < 6.1$  revealed by high-resolution spectroscopy (D’Odorico et al. 2013). The strongest system known in this redshift range at  $z_{\text{abs}} \sim 5.724$  (Ryan-Weber et al. 2006) inhabits an over-density of LAEs on scales of 10 comoving Mpc (Díaz et al. 2014) and has a galaxy counterpart at  $\sim 213$  pkpc (Díaz et al. 2015). This large distance to the C IV system is in tension with: (i) observations of the  $z \sim 2-3$  CGM (Steidel et al. 2010; Turner et al. 2014), (ii) predictions from cosmological simulations (Oppenheimer et al. 2009; Keating et al. 2016), and (iii) the typical wind speeds measured on star-forming galaxies (Shapley et al. 2003; Bradshaw et al. 2013; Hashimoto et al. 2013; Karman et al. 2014).

A simple explanation is that there are additional galaxies below the detection limit of Díaz et al. (2014). In favor of this idea, recent simulations modeling high redshift intergalactic absorption systems from García et al. (2017a) suggest that dwarf galaxies ( $-20.5 < M_{\text{UV}} < -18.8$  mag) are responsible for the metal absorptions observed at  $z \sim 5.7$ . These luminosities are fainter than the galaxy sample of Díaz et al. (2014). In particular, García et al. (2017a) reports that dwarf galaxies ( $M_{\star} \sim 2 \times 10^9 M_{\odot}$ ) with a  $\sim 100 \text{ km s}^{-1}$  wind speed could be the type of source associated to the C IV systems observed at  $z_{\text{C IV}} = 5.72419$ .

In this work, we have deepened our search for galaxies in the field of the QSO J1030+0524 using the Multi-Unit Spectroscopic Explorer (MUSE) on the Very Large Telescope (VLT). MUSE offers both the area and sensitivity to search for sub- $L_{\text{Ly}\alpha}^{\star}$  galaxies that could be responsible for the C IV absorptions. The main goals of this study are: *a)* to determine if there is a fainter galaxy closer to the strong C IV at  $z_{\text{C IV}} = 5.72419$  than the LAE from Díaz et al. (2015), and *b)* to search for galaxies near the other 10 C IV systems in the QSO’s line of sight. The first objective aims to address the hypothesis that faint galaxies closer to the line of sight are responsible for metals absorbers at  $z > 5$ . The second objective will contribute to the expansion of the sample of  $z > 5$  galaxy-C IV system pairs that are required to reconstruct the history of baryons across cosmic time.

Observations are described in Section 2. A detailed explanation of the detection method can be found in Section 3, and the resulting LAEs are presented in Section 4. The discussion in Section 5 reviews the the connection between star-forming galaxies and high-ionization absorption systems at high redshift. The conclusions can be found in Section 6. In this work we use *Planck 2014* cosmology ( $H_0 = 67.79 \pm 0.78 \text{ km s}^{-1} \text{ Mpc}^{-1}$ ,  $\Omega_{\text{M}} = 0.308 \pm 0.010$  and  $\Omega_{\Lambda} = 0.692 \pm 0.010$ , Planck Collaboration et al. 2014).

## 2 OBSERVATIONS

QSO J1030+0524 was targeted with the MUSE (Bacon et al. 2012) for 2 hours on April 10 2015 and 6 hours between January 7 2016 and January 10 2016<sup>1</sup>. The conditions during observation were good, with a seeing of  $\sim 1''$  reported during the first two hours and a seeing better than  $0.7''$  for the remaining 6 hours. The pixel scale is  $0.2 \text{ arcsec/pixel}$  and the spectral resolution is  $1.25 \text{ \AA/pixel}$ .

Each pointing employed the same observing strategy, where

<sup>1</sup> ESO programme 095.A-0714, PI Karman

we set up two observation blocks of 1440 seconds which followed a dither pattern with offsets of a fraction of arcsecond and rotations of 90 degrees to better remove cosmic rays and to obtain a better noise map. The total observation time of QSO J1030+0524 with MUSE, correcting for overheads, amounted to 6.4 hours.

We followed the data reduction as described in Karman et al. (2015) for both pointings, and refer to that paper for details. Here we provide only a brief description of the data reduction. We used the standard pipeline of MUSE Data Reduction Software version 1.0 on all of the raw data. This pipeline includes the standard reduction steps like bias subtraction, flat-fielding, wavelength calibration, illumination correction, and cosmic ray removal. The pipeline combines the processed raw data frames into a data-cube that includes the variance of every pixel at every wavelength. We subtracted the remainder of the sky at every wavelength in the obtained data-cube by measuring the median offset in 11 blank areas at every wavelength, and subtracting this from the entire field. The full width at half maximum (FWHM) was measured for the QSO and a second point-like object in the field, at various wavelengths. We confirmed the excellent observing conditions with a FWHM of  $\sim 0.7''$ , though slightly higher at the shorter wavelengths.

The field of QSO J1030+0524 was previously observed with the Advanced Camera for Surveys (ACS) on the *Hubble Space Telescope* (HST) in the  $i'$ -band (F775W) and the  $z'$ -band (F850LP) (Stiavelli et al. 2005). A description of the HST data reduction can be found in Díaz et al. (2011), although in this work we use these archival images for visual inspection only. We note, however, that none of the sources detected with MUSE was previously identified by studies of high redshift galaxies based on these HST images like Stiavelli et al. (2005) and Kim et al. (2009). As we will show in Section 4.2, most LAEs from the present work do not have a robust counterpart in the HST images. Indeed, these images are not deep enough to detect with sufficient significant the faint galaxies reported here.

### 3 DETECTION OF Ly $\alpha$ EMISSION LINE

The search for emission line galaxies was carried out in three different ways focusing on the redshifts around the C IV absorbers. We have not conducted a full blind search of the entire MUSE cube. The first sample of candidates was obtained by visual inspection (VI) as described in section 3.1. Then, the automatic detection (AD) described in section 3.2 returned a second independent sample of LAE candidates, which largely overlaps with the sample from VI. Finally, a third detection process was developed to search for sources in narrow-band images that contain emission lines only. We refer to this technique as ‘‘Differential Image Detection’’ (DID), which is described in section 3.3. This last procedure is more reliable so it was used for confirmation of candidates from the other two techniques.

#### 3.1 Visual inspection (VI)

The field of view (FoV) was divided in nine smaller sections and the data cube was inspected, frame by frame, in wavelength windows of 200 Å centered at the wavelength corresponding to Ly $\alpha$  (1215.668 Å) at the redshift of each of the 11 C IV absorption systems in Table 1, reported in D’Odorico et al. (2013, Table A3 therein). As a result, each of the nine small fields was surveyed in 11 windows in wavelength. The wavelength windows of 200 Å corresponds to  $\Delta v \sim 7400 \text{ km s}^{-1}$ , which largely exceeds the redshift range in

**Table 1.** C IV systems in the spectrum of QSO J1030+0524 from D’Odorico et al. (2013). Columns are: (1) reference number, (2) redshift, (3) equivalent width of the C IV doublet, and (4) column density.

| CIV ID         | $z(\text{C IV})$ (redshift) | $W_0(1548, 1550)$ (Å) | $\log_{10}(N_{\text{C IV}})$ ( $\text{cm}^{-2}$ ) |
|----------------|-----------------------------|-----------------------|---|
| 1              | 4.76671                     | 0.139                 | $13.13 \pm 0.03$                                  |
| 2              | 4.7966                      | 0.105                 | $13.30 \pm 0.04$                                  |
| 3              | 4.79931                     | 0.2                   | $13.37 \pm 0.02$                                  |
| 4              | 4.80107                     | 0.526                 | $13.46 \pm 0.01$                                  |
| 5              | 4.89066                     | 0.119                 | $13.21 \pm 0.02$                                  |
| 6 <sup>a</sup> | 4.9482                      | 0.49                  | $13.22 \pm 0.04$                                  |
|                |                             |                       | $13.77 \pm 0.01$                                  |
| 7 <sup>a</sup> | 5.5172                      | 0.61                  | $13.4 \pm 0.2$                                    |
|                |                             |                       | $13.92 \pm 0.05$                                  |
| 8              | 5.72419                     | 1.24                  | $14.52 \pm 0.08$                                  |
| 9 <sup>a</sup> | 5.7428                      | 0.79                  | $13.8 \pm 0.1$                                    |
|                |                             |                       | $13.89 \pm 0.09$                                  |
| 10             | 5.9757                      | 0.07                  | $13.1 \pm 0.3$                                    |
| 11             | 5.9784                      | 0.15                  | $13.4 \pm 0.2$                                    |

<sup>a</sup>Two components C IV absorption.

which a galaxy could be physically associated to the corresponding C IV system.

We searched for bright objects covering several spatial pixels that remain detectable in at least three consecutive frames (in the wavelength direction). Then we extracted a spectrum using a  $2''$  aperture (diameter). This was compared with 10 sky spectra obtained from regions of the FoV that have no objects to rule out sky residuals. As a result, five LAEs were identified with this technique. The next section describes the analysis of the data-cube with an independent automatic detection tool.

#### 3.2 Automatic Detection (AD)

The data-cube was analyzed with the *MUSE Python Data Analysis Framework* (MPDAF<sup>2</sup> 2.1, Bacon et al. 2016). For each C IV absorption system, a narrow wavelength section of 100 Å around the observed wavelength of Ly $\alpha$  was extracted from the cube. This small cube was scanned with MUSELET (MUSE Line Emission Tracker), which runs an automatic search for line-emission objects. The process creates narrow-band images and runs SExtractor (Bertin & Arnouts 1996) to detect isolated emission lines and emission line sources with continuum, using the default aperture size of  $1.6''$  (diameter). Default configuration parameters and a gaussian PSF convolution mask with FWHM= 2.0 pixels were used for source detection.

The output list of emission line sources with no continuum detection was sorted in velocity respect to the C IV to identify the closest candidates in the line-of-sight direction. Then, low redshift contaminants were removed based on the detection of other emission lines, as described below in section 3.4. This technique recovers three of the five LAEs from Visual Inspection and two new LAEs.

#### 3.3 Differential Image Detection (DID)

This section describes a procedure to highlight emission line objects in the field of view, by removing all other sources using narrow-band (NB) images. For every C IV system in Table 1, the process was

<sup>2</sup> <http://mpdaf.readthedocs.io>

the following. A small cube of  $10 \text{ \AA}$  ( $\sim 50\text{--}75 \text{ km s}^{-1}$  rest-frame) with central wavelength corresponding to  $\text{Ly}\alpha$  at the redshift of the C IV absorption, was collapsed in wavelength direction using a variance-weighted sum with weights  $w_i = 1/\sigma_i^2$  for the  $i$ -th pixel, to create a NB image corresponding to rest-frame  $\text{Ly}\alpha$ . The  $\text{Ly}\alpha$  forest (Lyf) and the UV continuum (UV) were sampled with two small ( $10 \text{ \AA}$ ) cubes shifted  $40 \text{ \AA}$  to the blue and  $40 \text{ \AA}$  to the red of  $\text{Ly}\alpha$ , respectively. These two cubes were collapsed to produce NB images of the  $\text{Ly}\alpha$  forest and the UV continuum. No filter transmission was applied. Then, one NB image was subtracted from another to produce a differential image (DI). The following DIs were calculated: (NB( $\text{Ly}\alpha$ )-NB(UV)) and (NB( $\text{Ly}\alpha$ )-NB( $\text{Ly}\alpha_{\text{forest}}$ )), in which most sources are removed while the sources with flux excess in the NB( $\text{Ly}\alpha$ ) (e.g. with an emission line) are revealed.

Figure 1 presents the FoV of MUSE with QSO J1030+0524 at the center. The image on the left is centered at  $\lambda \sim 8176 \text{ \AA}$ , which is the wavelength of  $\text{Ly}\alpha$  at  $z \sim 5.725$ . It has tens of sources, some of them are obvious (bright) low-redshift and galactic sources, but most of them are faint sources. The image on the right panel is (NB( $\text{Ly}\alpha$ )-NB(UV)), where the UV continuum was subtracted from the  $\text{Ly}\alpha$  line. In this image, most sources in the field are completely removed, while LAE #5 (see Table 2) is clearly visible.

DIs were thoroughly examined to detect all possible sources both visually and with SExtractor. The list of SExtractor detections was obtained using default configuration parameters except for *DETECT\_MINAREA* = 3 pixels, *DETECT\_THRESH* = 1.5 and *SEEING\_FWHM*=0.7. Each detection was analyzed to remove lower redshift interlopers. After this process, only one or two LAE candidates were left per C IV system. Overall, this method returns six sources (LAEs #1, 2, 3, 5 and 6), and only one of them (LAE #6) was not detected with other methods.

In addition, DID was used to test other candidates from AD and VI that lie at  $\sim 800 \text{ km s}^{-1}$  from a C IV absorption (LAEs 4, 7 and 8). The analysis confirmed these three detections and demonstrates the agreement between the techniques. Therefore, the final sample of eight LAEs in Table 2 is considered consistently detected by the DID technique.

### 3.4 Removal of low redshift contaminants

For every emission line detection, the spectrum was thoroughly inspected for additional emission lines that would reveal a low redshift contaminant. In this exercise, it was assumed that the line was  $\text{H}\alpha$ ,  $\text{H}\beta$ , [O III](5007Å), [O III](4958Å), or [O II](3727Å). For each case, the wavelength of other optical emission lines was calculated. Then, we examined the cube (3D) and the spectrum (1D) to assess the presence of additional emission lines. In this process, several emitters of [O III], [O II], and  $\text{H}\alpha$  have been identified at  $z = 0.33, 0.42, 0.567, 0.825, 1.01, 1.03$  and  $1.2$ . The sources that show no other emission line are the LAEs in the sample of Table 2.

## 4 RESULTS

### 4.1 LAE candidates

We report the detection of 8 LAE candidates in the datacube. The positions are indicated in Figure 2 and presented in Table 2, along with the redshift, angular distance to the QSO l.o.s., impact parameter and radial velocity to the C IV system, the total line flux,  $\text{Ly}\alpha$  luminosity, rest-frame equivalent width ( $\text{EW}_0$ ) of the emission line (assuming it is  $\text{Ly}\alpha$ ) and the skewness of the line profile.

Figure 3 presents a closer look at each galaxy with thumbnails of  $10''$  by  $10''$ , centered at the position of the corresponding detection, and the 2D spectrum extracted from the data-cube. The first two columns from left to right, NB( $\text{Ly}\alpha$ ) and UV continuum, are images extracted from the data-cube. They sample the  $\text{Ly}\alpha$  emission and the UV continuum between  $1220\text{ \AA}$  to  $1300\text{ \AA}$ . The latter was obtained from multiple wavelength windows defined to avoid strong sky emission residuals which are clearly visible in the 2D spectrum of most sources. The third and fourth columns are ACS/HST images in the  $i'$  and  $z'$  bands, respectively. Only LAE #5 can be identified in the  $z'$ -band image ACS/HST. We ran SExtractor several times using different detection configurations and weight types, and we found that none of the other sources have detectable  $z'$ -band counterparts.

The emission lines were confirmed in the 2D and 1D spectra. Figure 3 shows the 2D spectra extracted using virtual slits of  $0.7$  to  $1''$  width, which are displayed in the same figure. The emission lines are indicated with blue arrows.

The 1D spectra were extracted using circular apertures of diameter equal to  $2\times$  the FWHM of the sources measured by SExtractor in the detection image. The 1D spectrum and the aperture of extraction of each object are presented in Figures 4 to 11. The comparison sky background is represented with a cyan-filled area. It was extracted from an annular aperture centred on the source, with a  $2''$  inner radius and a  $5''$  outer radius. All foreground objects where masked out before computing the mean flux density in the sky aperture.

The emission redshift reported in Table 2 was determined from the blue edge of the emission line profile assuming that most of the line flux is heavily absorbed by neutral hydrogen in the emitting galaxy (e.g. Verhamme et al. 2008). The velocity difference between the LAE and the C IV system is calculated as:

$$\Delta V(\text{C IV} - \text{Ly}\alpha) = \left(1 - \frac{\lambda_{obs}}{1215.668 \times (1 + z_{\text{C IV}})}\right)c \quad (1)$$

where  $\lambda_{obs}$  is the observed wavelength of the emission line,  $z_{\text{C IV}}$  is the redshift of the corresponding C IV system, and  $c$  is the speed of light in the vacuum. The impact parameter (or transversal distance) in proper kpc is obtained as:  $\rho = \delta\theta/g(z_{\text{Ly}\alpha})$  where  $\delta\theta$  is the angular separation between the corresponding LAE and the QSO, and  $g(z_{\text{Ly}\alpha})$  is the scale factor in  $''/\text{pkpc}$  at the redshift of the  $\text{Ly}\alpha$  emission.

The weighted skewness ( $S_w$ ) of the line profile, which quantifies the asymmetry of the emission line, was measured as defined in (Kashikawa et al. 2006). Five LAE candidates have positive skewness which is associated with the absorption by neutral hydrogen on the blue side of the line profile. The remaining three candidates, those with negative skewness, are the faintest sources in the sample. In particular, the large error on  $S_w$  for LAE #6 results from a faint emission line whose symmetry is affected by noise (1D spectrum in Figure 9). The other two objects with negative skewness are LAE #1 and LAE #4. The effect of including these two candidates in the analysis will be considered in Section 5.

The total line flux is calculated from the integral over the line profile, which is indicated in the central panels of Figures 4 to 11 with a grey-shaded area between green lines. The integral was approximated by a weighted sum of the form:

$$F_{\text{Ly}\alpha} = \frac{\sum f_i w_i \Delta\lambda}{\sum w_i} \times n_{pix} \quad (2)$$

where  $f_i$  is the flux density of the  $i$ -th pixel,  $w_i$  are the weights calculated from the variance spectrum as  $w_i = 1/\sigma_i^2$ , and  $\Delta\lambda = 1.25$

**Table 2.** LAEs from the search with MUSE. Columns are: (1) C iv system identification, (2) LAE reference number, (3) right ascension hh:mm:ss.ss (J2000), (4) declination  $\pm$ dd:mm:ss.s (J2000), (5) redshift assuming the blue edge of the line profile is 1215.668 Å, (6) angular distance to the QSO in arcseconds, (7) transversal distance C iv absorption in proper kpc, (8) line of sight velocity to the C iv absorption in km s<sup>-1</sup>, (9) total line flux in erg s<sup>-1</sup> cm<sup>-2</sup>, (10) luminosity of the emission line in erg s<sup>-1</sup> assuming it is Ly $\alpha$ , (11) lower limits on the rest-frame equivalent width in Å, and (12) weighted skewness.

| System | LAE# | RA          | Dec         | $z(\text{Ly}\alpha)$ | $\delta\theta$ | $\rho$ | $\Delta V$ | $F_{\text{Ly}\alpha}/10^{-18}$ | $L_{\text{Ly}\alpha}/10^{41}$ | $\text{EW}_0$ | $S_w$          |
|--------|------|-------------|-------------|----------------------|----------------|--------|------------|--------------------------------|-------------------------------|---------------|----------------|
| C iv 6 | 1    | 10:30:28.56 | +05:25:11.4 | 4.947                | 27.242         | 176    | 71         | $3.1 \pm 0.4$                  | $8.3 \pm 1.1$                 | $> 14$        | $-1.4 \pm 0.8$ |
| C iv 7 | 2    | 10:30:26.32 | +05:25:09.7 | 5.518                | 18.672         | 114    | 2          | $4.4 \pm 0.5$                  | $15.4 \pm 1.7$                | $> 4$         | $0.6 \pm 0.6$  |
|        | 3    | 10:30:26.64 | +05:24:56.4 | 5.518                | 6.807          | 42     | 2          | $7.4 \pm 0.5$                  | $25.5 \pm 1.6$                | $> 8$         | $2.0 \pm 0.6$  |
|        | 4    | 10:30:26.52 | +05:24:35.4 | 5.530                | 21.419         | 131    | -566       | $2.8 \pm 0.4$                  | $9.5 \pm 1.4$                 | $> 4$         | $-2.7 \pm 0.9$ |
| C iv 8 | 5    | 10:30:27.68 | +05:24:19.8 | 5.721                | 36.411         | 218    | 127        | $14.4 \pm 0.3$                 | $52.6 \pm 1.1$                | $> 44$        | $4.3 \pm 0.7$  |
|        | 6    | 10:30:26.99 | +05:24:56.1 | 5.720                | 1.627          | 10     | 172        | $3.4 \pm 0.3$                  | $12.7 \pm 1.1$                | $> 8$         | $-1.9 \pm 1.6$ |
| C iv 9 | 7    | 10:30:28.96 | +05:24:53.1 | 5.758                | 27.887         | 167    | -639       | $8.5 \pm 0.3$                  | $32.1 \pm 1.1$                | $> 27$        | $4.0 \pm 1.1$  |
|        | 8    | 10:30:27.15 | +05:25:07.9 | 5.758                | 12.854         | 77     | -639       | $8.0 \pm 0.3$                  | $30.4 \pm 1.1$                | $> 15$        | $8.0 \pm 1.5$  |

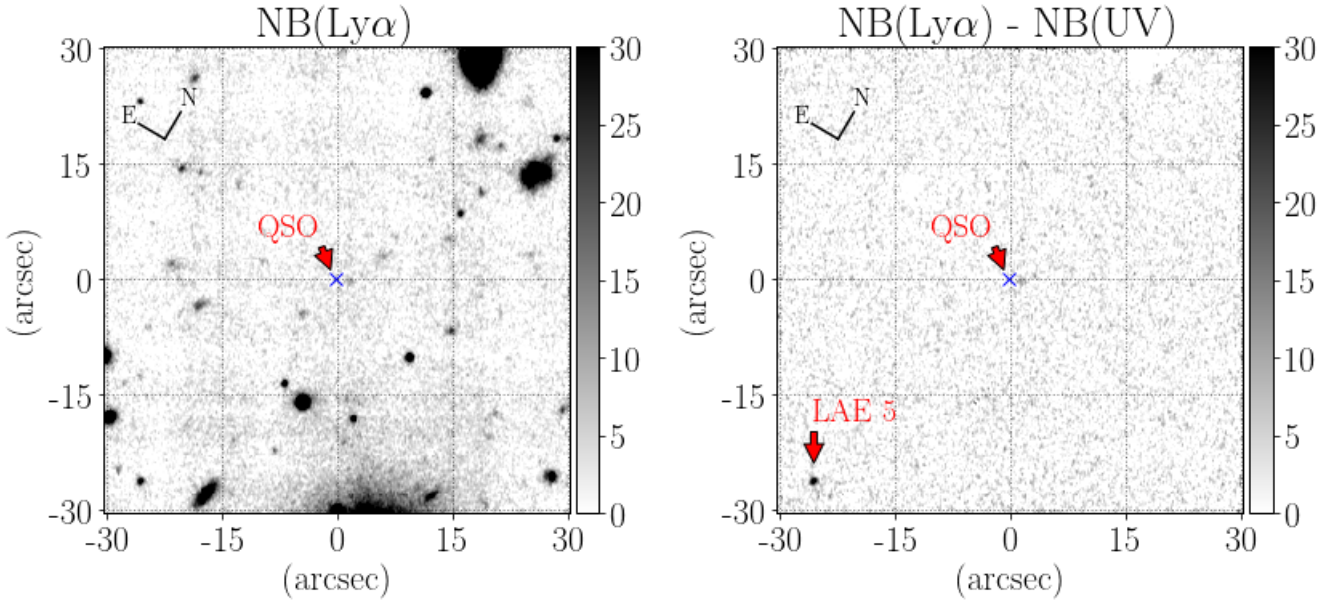


**Figure 1.** LAE #5 in MUSE’s field of view. The NB image on the left has a central wavelength corresponding to Ly $\alpha$  at  $z = 5.721$  and the image on the right is a differential image NB(Ly $\alpha$ )-NB(UV).

Å/pix is the spectral resolution. The errors reported in Table 2 are estimated from:

$$\delta F_{\text{Ly}\alpha} = \frac{\sum w_i^2}{(\sum w_i)^2} \times 10^{-18}. \quad (3)$$

In all candidates, the continuum flux density redder than Ly $\alpha$  is an upper limit because is below the detection limit of the data given by the error spectrum, or at least comparable to the flux level measured in the sky aperture. The continuum was estimated as the average of several windows in wavelength to avoid high skylines residuals the best we could, and for each window the mean flux density was obtained from a weighted sum:

$$f_{\text{UV}} < \left\langle \frac{\sum_i f_{i,k} w_{i,k}}{\sum_i w_{i,k}} \right\rangle, \quad (4)$$

where  $f_{i,k}$  and  $w_{i,k}$  are the flux density and the weight of the  $i$ -th pixel and the  $k$ -th window.

Finally, the lower limits on the rest-frame Ly $\alpha$  equivalent width

( $\text{EW}_0$ ) are obtained as:

$$\text{EW}_0 > \frac{F_{\text{Ly}\alpha}}{f_{\text{UV}}} \times \frac{1}{(1+z)}. \quad (5)$$

## 4.2 Individual LAEs

Figures 4 to 11 present three thumbnails of 10 arcsec wide in the top row, centered on the corresponding candidates: the NB(Ly $\alpha$ ) image (left panel), the aperture for extraction of the 1D spectrum of the source (middle panel) and the aperture of extraction of the sky for comparison (right panel). The center panel presents the 1D spectrum obtained from the source aperture (top middle) with solid black line. The error spectrum is represented by the blue dashed line and the 1D spectrum from the sky aperture (top right) is presented as filled cyan spectrum. The vertical dotted lines indicate the limits of the line profile considered to compute the total flux reported in

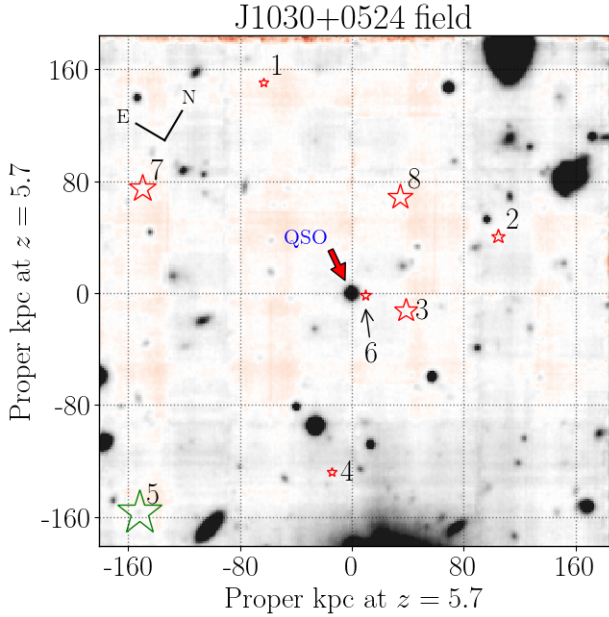


**Figure 2.** Position of the LAEs of Table 2 in MUSE’s FoV. The background QSO is at the center of the field, the red and green star symbols indicate the positions of the LAEs and the size of the symbol is proportional to the Ly $\alpha$  line flux.

Table 2. Finally, in the bottom panel we present the sky spectrum for reference, in an arbitrary scale.

#### 4.2.1 LAE 1

This candidate was detected at 27.242'' from the QSO and is the only LAE for the C IV system at  $z_{\text{CIV}} = 4.9482$ . The emission line is detected at  $z_{\text{CIV}} = 4.947$ , which puts this object at 176 pkpc and  $\Delta V = 70.8 \text{ km s}^{-1}$  from the C IV system. The 1D spectrum of Figure 4 shows a faint emission line that is absent in the comparison sky spectrum. The skewness of the line profile is negative, but it should be noted that a fraction of the object emission line could be coincidental with the strong sky emission line at  $\lambda = 7240 \text{ \AA}$  and thus not included in the calculation of the line flux.

#### 4.2.2 LAE 2

This object lies at 18.672'' from the QSO sight-line with an emission redshift of  $z_{\text{BLUE}} = 5.518$ , which puts it at 114 pkpc from the C IV system at  $z_{\text{CIV}} = 5.5172$ . The emission is observed between bright sky emission lines (Figure 5), therefore the redshift estimate is limited and the asymmetry of the line profile cannot be measured with high confidence.

#### 4.2.3 LAE 3

LAE #3 is also at  $z = 5.518$ , making it a neighbor of LAE #2. It lies at 6.807'' (42 pkpc) from the QSO line of sight, thus it is closer to the C IV system at  $z_{\text{CIV}} = 5.5172$  than LAE #2. In the close view in Figure 3, the object is clearly seen in NB(Ly $\alpha$ ) but there is no evidence in the rest-frame UV. The 2D spectrum shows an emission line brighter than LAE #2 but similarly affected by the sky emission.

#### 4.2.4 LAE 4

LAE #4 is a faint source at 21.419'' from the QSO sight-line. If it is Ly $\alpha$  the redshift is  $z_{\text{BLUE}} = 5.530$  and the impact parameter is 131 pkpc. Thus, it is near the C IV system at  $z_{\text{CIV}} = 5.5172$ . Figure 3 shows a faint detection in NB(Ly $\alpha$ ) and nothing in the other images. The emission line is confirmed in the 2D and 1D spectra (Figure 7). The velocity difference to the C IV system is larger than  $500 \text{ km s}^{-1}$ , and the asymmetry of the line is negative which could be indicative of a lower redshift interloper.

#### 4.2.5 LAE 5

This is the brightest LAE in the sample. It was previously reported by Díaz et al. (2014) and confirmed in Díaz et al. (2015). In this work, we measure an angular distance to the QSO line of sight of 36.411'' and a redshift of  $z_{\text{Ly}\alpha} = 5.721$ . As a result, it lies at 218 pkpc from the strong C IV system at  $z_{\text{CIV}} = 5.72419$ . LAE #5 is clearly seen in the z'-band image in Figure 3 and, like all other source in the sample, LAE #5 is detected in NB(Ly $\alpha$ ) but not detected in the i'-band, which is typical of high- $z$  galaxies. The 2D and 1D spectra are the highest signal-to-noise of the sample and the asymmetry of the line is obvious in both representations (Figure 8). Line flux measurements, redshift,  $S_w$  and  $\text{EW}_0$  estimates are in agreement with previously reported values.

#### 4.2.6 LAE 6

This LAE candidate is at 1.627'' from the QSO line of sight. The emission line is consistent with Ly $\alpha$  at  $z_{\text{BLUE}} = 5.720$  that would make it the closest LAE to the C IV system at  $z_{\text{CIV}} = 5.72419$ , and a satellite of LAE #5. The object is faint in NB(Ly $\alpha$ ) and there is no trace of it in other images. The virtual slit in Figure 3 captures the LAE and part of the QSO light. As a result, the 2D spectrum shows the emission line of LAE #6 and the Ly $\alpha$  forest in the QSO spectrum. The 1D spectrum in Figure 9 shows a faint emission line in a region free of strong sky residuals. The signal is spread across several adjacent pixels in the sky (e.g. NB(Ly $\alpha$ )) and in wavelength direction (2D and 1D spectra). The low signal-to-noise of the emission line, which seems quite symmetric, results in large errors in  $S_w$ . Thus, asymmetry should not be used to evaluate the nature of the emission line.

#### 4.2.7 LAE 7

This galaxy is a solid detection, the asymmetry of the line profile is consistent with high- $z$  Ly $\alpha$  at  $z_{\text{BLUE}} = 5.758$ , which is at  $\Delta V \sim -638.6 \text{ km s}^{-1}$  to the C IV system at  $z_{\text{CIV}} = 5.7428$ . LAE #7 is at 27.887'' (167 pkpc) to the East of the QSO sight-line and it is only detected in NB(Ly $\alpha$ ) like most of the sample. The emission line is not contaminated by sky residuals, and the 2D and 1D spectra clearly show an asymmetric profile confirmed by  $S_w$  (Table 2).

#### 4.2.8 LAE 8

This LAE is at the same redshift of LAE #7 ( $z_{\text{BLUE}} = 5.758$ ) and the line profile supports the LAE identification. It is at 12.854'' (77 pkpc) to the North of the QSO sight-line, thus it is the closest LAE to the C IV system at  $z_{\text{CIV}} = 5.7428$ . The emission in the 2D spectrum is typical of high- $z$  LAEs and the 1D spectrum confirms the asymmetry of the line with a skewness of  $S_w = 8.0 \pm 1.5$ .

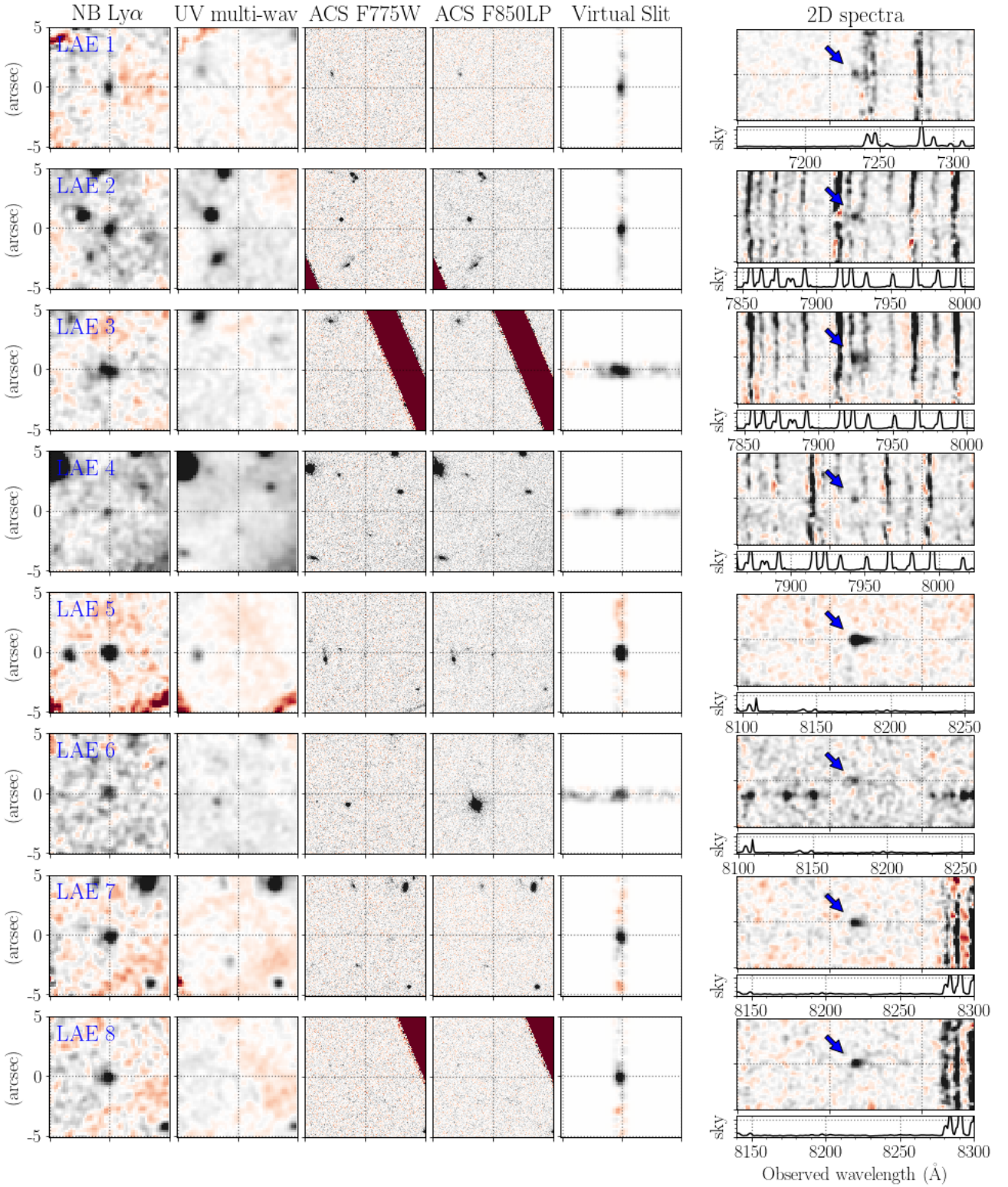


**Figure 3.** LAE candidates. Images from left to right are: NB(Ly $\alpha$ ), UV continuum extracted from multiple wavelength windows,  $i'$ -band (ACS/HST),  $z'$ -band (ACS/HST), the slit used for extraction of the 2D spectrum, and the 2D spectrum with an arrow indicating the position of the emission line and a sub-plot showing the emission spectrum of the sky for reference.

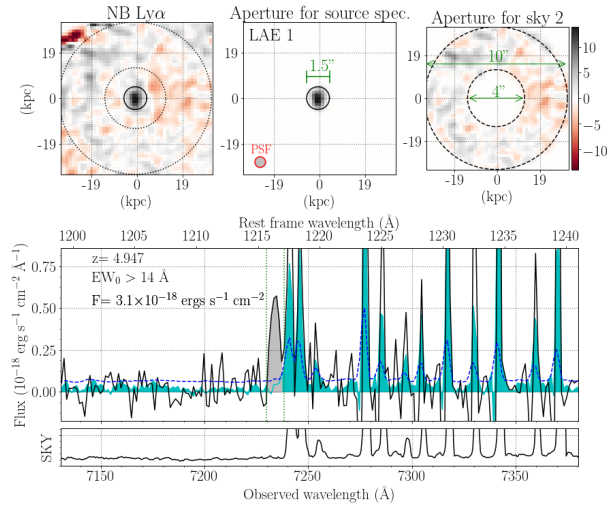


**Figure 4. LAE #1.** The top figures show the NB(Ly $\alpha$ ) image (left), the aperture used for extraction of the 1D spectrum (center) and the aperture used for the extraction of the sky spectrum (right) for comparison. The middle panel shows the 1D spectrum of the LAE with a black line and the 1D spectrum of the sky with a cyan-filled area. The Ly $\alpha$  emission line is indicated by the grey-filled area between dotted green vertical lines. The error spectrum is the blue dashed line.

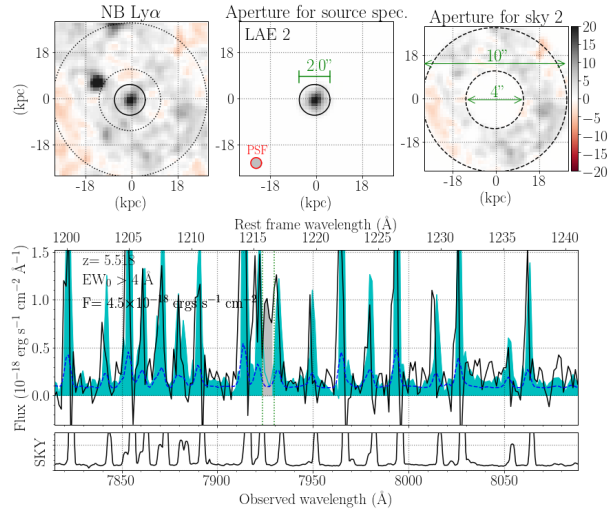


**Figure 5. LAE #2.** Description as per Figure 4.

### 4.3 Comparison with previous studies of the same field

The field of the QSO J1030+0524 has been studied before with different instruments. Here we use MUSE data to review the LAE candidates identified by previous works. Figure A3 shows MUSE’s FoV, the position of the LAE candidates in Table 2, the position of the two LAE candidates in Cai et al. (2017) with blue circles, the position of the candidates from Díaz et al. (2011) with blue diamonds, and the LAE previously confirmed by Díaz et al. (2015).

#### 4.3.1 Díaz et al. (2011)

The first attempt to search for galaxies at the redshift of the C iv systems is the spectroscopic study of Díaz et al. (2011), which followed up three galaxy candidates from Stiavelli et al. (2005),

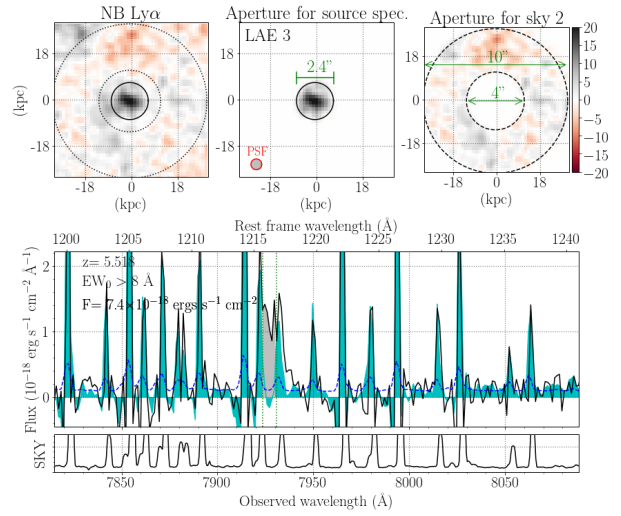


**Figure 6. LAE #3.** Description as per Figure 4.

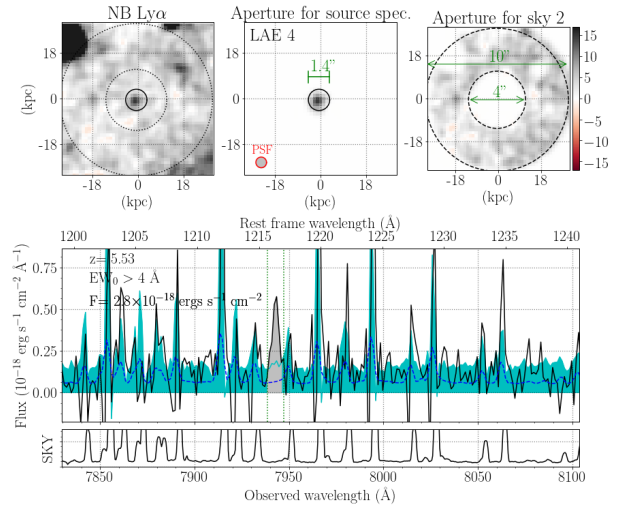


**Figure 7. LAE #4.** Description as per Figure 4.

referred to as Target 1, 2 and 3. Target 1 (J103024.08+052420.41) was confirmed by its Ly $\alpha$  emission in Stiavelli et al. (2005) and then by Díaz et al. (2011) at  $z_{em} \sim 5.973$ . We recalculated the redshift using our definition based on the bluest pixel of the Ly $\alpha$  line profile and found  $z_{BLUE} = 5.968$  (Figure 13). This LAE is at 57.163’’ (335 pkpc) to the South-West of the QSO sight-line, thus it is outside MUSE’s FoV but it lies within 500 km s $^{-1}$  of the two C iv systems at  $z_{CIV} = 5.9757$  and 5.9784, for which no other galaxy candidate was identified in the datacube. Following the identification number assigned to the LAEs in the sample, in this work we will refer to this galaxy as LAE #9 (see Table 3 for details).

Target 2 (J103027.98+052459.51,  $z_{em} = 5.676$ ) and Target 3 (J103026.49+052505.14,  $z_{em} = 5.719$ ) are both inside the MUSE’s FoV but neither were recovered by our detection procedure based on Ly $\alpha$  line emission. In Appendix A, Figures A1 and A2 present images of each object from different observing campaigns. The top row of images correspond to MUSE data. The Blue and the Red images are broad-band images that sample the rest-frame wavelength range bluer and redder than Ly $\alpha$ , respectively, with a bandwidth defined in 1000 km s $^{-1}$ . The object cannot be identified in these im-



**Table 3.** LAE outside the FoV of MUSE. Columns are: (1) reference number, (2) right ascension hh:mm:ss.ss, (3) declination  $\pm$ dd:mm:ss.s, (4) redshift assuming the blue edge of the line profile, (5) angular distance to the QSO, (6) total line flux and (7) luminosity of Ly $\alpha$ .

| ID     | RA<br>(J2000) | Dec<br>(J2000) | $z_{\text{BLUE}}$<br>(redshift) | $\delta\theta$<br>(") | $\rho$<br>(pkpc) | $F_{\text{Ly}\alpha}$<br>( $\times 10^{-18}$ erg s $^{-1}$ cm $^{-2}$ ) | $L_{\text{Ly}\alpha}$<br>( $\times 10^{41}$ erg s $^{-1}$ ) |
|--------|---------------|----------------|---------------------------------|-----------------------|------------------|---|---|
| LAE #9 | 10:30:24.08   | +05:24:20.41   | 5.968                           | 57.163                | 335              | $9.3 \pm 0.8$   | $38.3 \pm 3.4$  |

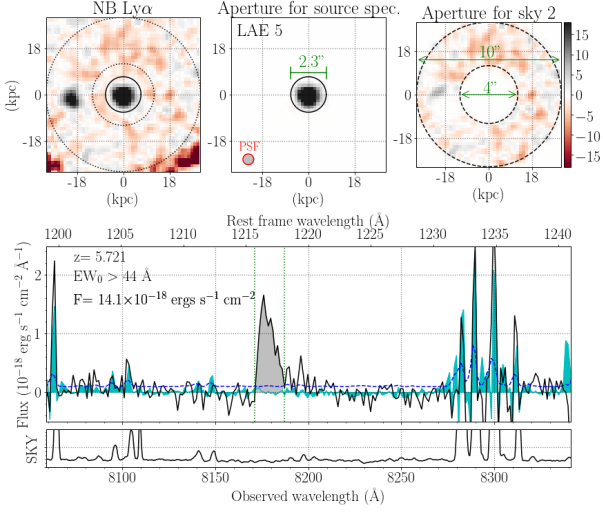


**Figure 8.** Spectrum of LAE 5. Description as per Figure 4.

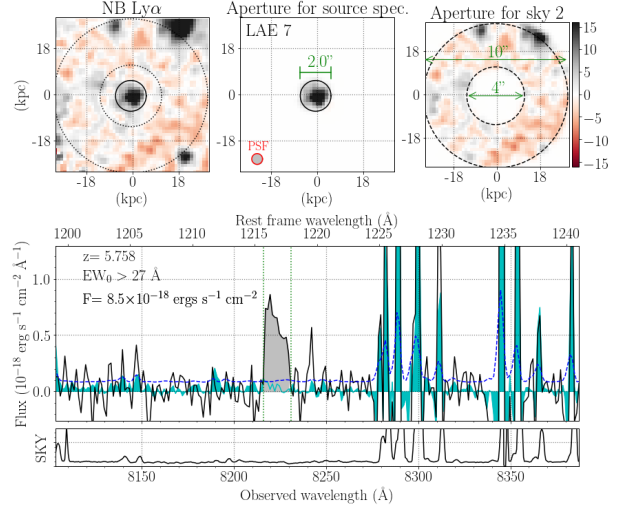


**Figure 10.** LAE #7. Description as per Figure 4.

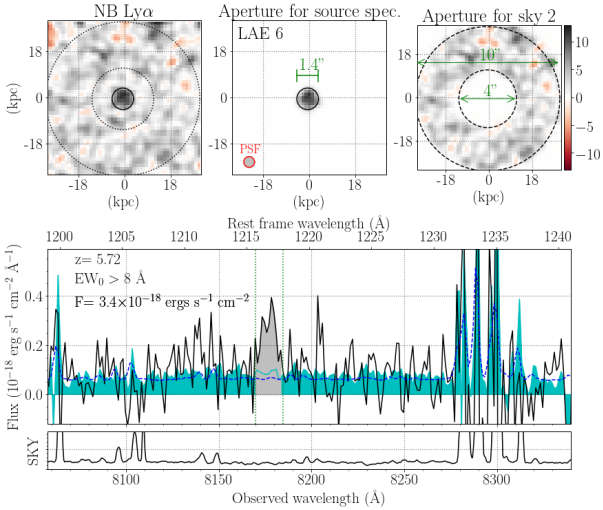


**Figure 9.** LAE #6. Description as per Figure 4.

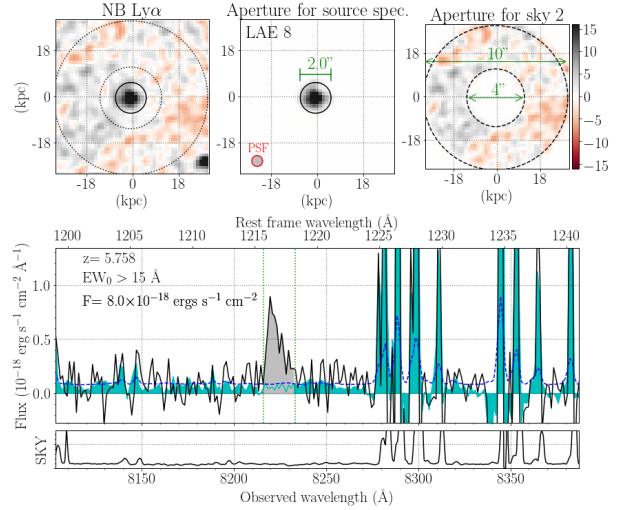


**Figure 11.** LAE #8. Description as per Figure 4.

ages and no emission line is detected in the 2D spectrum despite the flux value reported by Díaz et al. (2011),  $F_{\text{Ly}\alpha} = 4.9 \pm 1.1 \times 10^{-18}$ , is above our detection limit.

The second row in Figure A1 shows SuprimeCam images in the photometric bands  $R_c$ , NB(C IV),  $i'$  and  $z'$  from Díaz et al. (2014). The third row shows ACS HST images (Stiavelli et al. 2005) in  $i'$ -band (F775W) and  $z'$ -band (F850LP). As reported in Díaz et al. (2014), Target 2 is detected in  $z'$  with  $S/N \geq 5$  and the signal in the bluer images is too low to confirm a detection, resulting in red ( $i'-z'$ ) colors and supporting the high- $z$  nature of the object. However, the lack of Ly $\alpha$  emission line contradicts the original classification of

this object as an LAE. Therefore, we will not include this candidate in our current analysis.

Figure A2 presents Target 3 which has already been ruled out as high- $z$  source by Díaz et al. (2014) based on the detection of the source in the  $R_c$ -band with  $S/N \sim 4$  and magnitude  $R_c = 26.6 \pm 0.3$ . Here we review the SuprimeCam images in the second row of Figure A2 where the source can be identified in the  $R_c$  thumbnail. The object is hardly detected in the blue and red MUSE images, and there is no evidence of an emission line in the 2D spectrum. This confirms that Target 3 is not at  $z_{em} = 5.719$  and it will not be considered in the future.

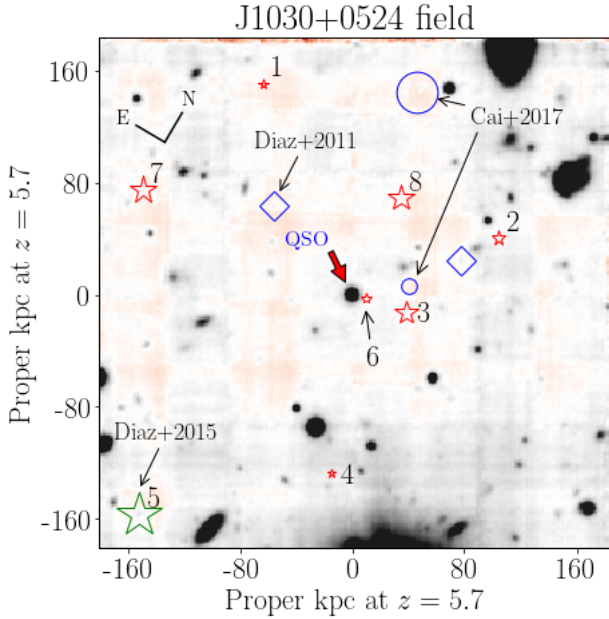


**Figure 12.** Same as Figure 2 including the two detections from Cai et al. (2017) (circles) and two from Díaz et al. (2011) (diamonds). The circle size is scaled to the flux expected for the Ly $\alpha$  luminosity reported in Cai et al. (2017).

In summary, we confirm a lack of Ly $\alpha$  emission line at the flux level reported in Díaz et al. (2011) for their Target 2 and 3, the latter previously ruled-out by Díaz et al. (2014). Also, we include their Target 1 in the current analysis as LAE #9.

#### 4.3.2 Díaz et al. (2014, 2015)

The projected distribution of LBGs brighter than  $z' = 25.5$  ABmag in the field J1030+0524 revealed that the candidate closest to the QSO line of sight is at  $\sim 5.1$  cMpc ( $\sim 761$  pkpc). The absence of bright LBG candidates in the proximity of the C IV system suggests that fainter galaxies had to be present at closer distances from the strong C IV system at  $z \sim 5.7$  (Díaz et al. 2014). In addition, Díaz et al. (2015) confirmed the closest NB-selected LAE brighter than NB  $\sim 25.5$  ABmag at  $\sim 213$  pkpc from the C IV system, but such a distance is also too large to account for metal enrichment given the short age of the Universe at  $z \sim 5.7$ . As a result, the expectation was that the closest galaxies remained below the detection limit.

The new galaxies identified with MUSE and reported in this work have no continuum detected. Thus, is in agreement with the large-scale photometric study of Díaz et al. (2014), we confirm the absence of UV-bright galaxies within  $\sim 250$  pkpc not only at  $z \sim 5.7$  but also for all the other C IV systems in the line of sight. Finally, the current sample is a confirmation of the presence of several very faint galaxies ( $L_{\text{Ly}\alpha} \sim 0.9 - 5.2 \times 10^{42}$  ergs s $^{-1}$ , see Section 4.6) within 200 pkpc of C IV systems at  $z > 5.5$ , which agrees with the conclusion from Díaz et al. (2015) at  $z \sim 5.7$ .

#### 4.3.3 Cai et al. (2017)

Based on HST imaging, Cai et al. (2017) reported two narrow-band selected LAE candidates for the C IV systems at  $z_{\text{C IV}} = 4.948$  and 5.744. The estimates of the Ly $\alpha$  luminosity of these candidates are within the detection limit of our sample and they should be

detectable in the data cube. We reviewed the data at the coordinates reported in Cai et al. (2017) and found that the first candidate (Object 1, RA=10:30:26.746 Dec.=+5:24:59.76), which was associated with the C IV system at  $z_{\text{C IV}} = 5.744$ , is 3.1'' away from LAE #3 (see Figure A3) at  $z_{\text{BLUE}} = 5.518$ . The left image in Figure A3 is a NB(Ly $\alpha$ ) image at the wavelength of Ly $\alpha$  at  $z=5.744$ . There is no evidence of an emission line at the coordinates for Object 1 in this image. We also analyzed the white image integrated over the full wavelength range, the 1D spectrum and the 2D spectrum and we find no evidence of an emission line. However, candidate LAE #3 in our sample is 3.1'' from the position of Object 1. The center panel of Figure A3 shows a NB(Ly $\alpha$ ) image at the redshift of LAE #3. The Ly $\alpha$  emission of LAE #3 is detected at  $\lambda \sim 7924$  Å which is in the blue wing of the NB filter F853N used in Cai et al. (2017). Therefore, it is possible that we have identified the same object, in which case the first LAE candidate in Cai et al. (2017) would correspond to LAE #3 in our sample (Table 2), and its true redshift is  $z_{\text{BLUE}} = 5.518$ .

The second object (RA= 10 : 30 : 26.746, Dec.= +05 : 24 : 59.76) was identified in the data cube, although it shows a small offset in our world coordinate system. Figure A4 presents a close look at this galaxy. The top left image, where the object is detected near the center of the field, was obtained by combining all frames at wavelengths bluer than the rest-frame Lyman limit ( $\lambda < 912$  Å) at  $z_{\text{C IV}} = 4.948$ . The top center shows the NB image for Ly $\alpha$  at  $z_{\text{em}} = 4.948$  and there is no emission line on it. The 2D spectrum in the middle panel shows a faint continuum signal across the wavelengths range that would correspond to Ly $\alpha$  at  $z_{\text{em}} = 4.948$ . In this case, we can rule out the high- $z$  LAE hypothesis based on the detection of flux at rest frame  $\lambda < 1216$  Å.

#### 4.4 Environment of absorption systems

The X-Shooter spectrum of the QSO J1030+0524 revealed 11 C IV systems in the range  $z_{\text{C IV}} = 4.757-6.187$  (D'Odorico et al. 2013), which are listed in Table 1. In the sample, there are three systems with double C IV absorptions (C IV ID: 6, 7 and 9), one strong system (C IV 8,  $\log_{10}(N_{\text{C IV}}[\text{cm}^{-2}]) > 14.0$ ), and seven weaker C IV systems (C IV 1, 2, 3, 4, 5, 10 and 11,  $\log_{10}(N_{\text{C IV}}[\text{cm}^{-2}]) < 13.5$ ). The search for LAEs in the environment of these absorptions resulted in at least one LAE for each C IV system with  $\log_{10}(N_{\text{C IV}}[\text{cm}^{-2}]) > 13.5$  and multiple LAEs for the systems at  $z_{\text{C IV}} > 5.5$ .

One of the main results is summarized in Figure 14, it shows the impact parameter of the LAEs with respect to the line of sight as a function of redshift. The C IV systems are represented by open squares of sizes divided into three bins in column density. The LAEs are represented by star symbols with sizes proportional to the flux of the Ly $\alpha$  emission, and labels indicating the ID numbers. Green symbols correspond to galaxies previously known and red symbols are new detections. The dashed lines indicate the radial distance from the position of the QSO in the center of MUSE's FoV to the edge and the corner of the FoV. This shows that MUSE can cover about  $\sim 200-280$  pkpc and within this distance we have found multiple LAEs for three C IV systems at  $z > 5.5$ . Also, all C IV systems with  $\log_{10}(N_{\text{C IV}}[\text{cm}^{-2}]) > 13.5$  at least one LAE candidate within  $\sim 200-280$  pkpc.

Providing a closer look, Figure 15 shows the line of sight velocity to the corresponding C IV vs. impact parameter. In each case, the redshift of the C IV is indicated in the top left corner. The C IV systems are represented by open blue squares at  $\Delta V(\text{C IV} - \text{Ly}\alpha) = 0$  that scale with column density as in Figure 14. The presence of C II and Si IV is indicated with open red squares and filled cir-

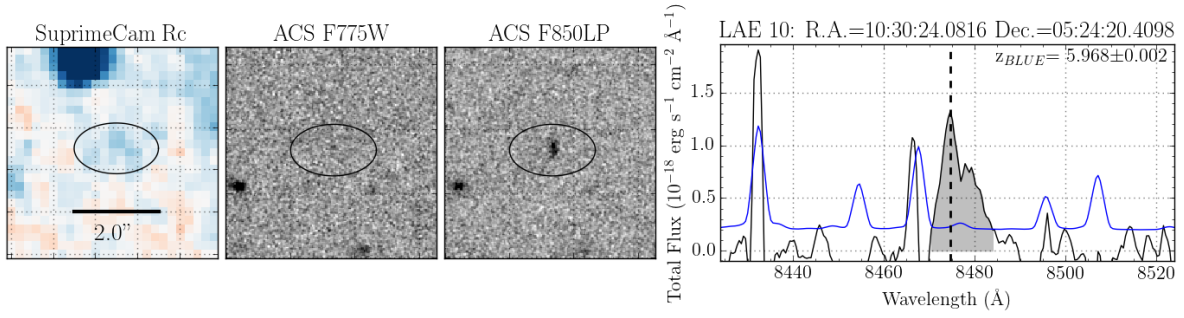


**Figure 13.** Thumbnail images and 1D spectrum of LAE #9. From left to right: Rc band (Subaru),  $i'$ -band (HST),  $z'$ -band (HST), and the spectrum from DEIMOS (Keck). The error spectrum is the blue line.

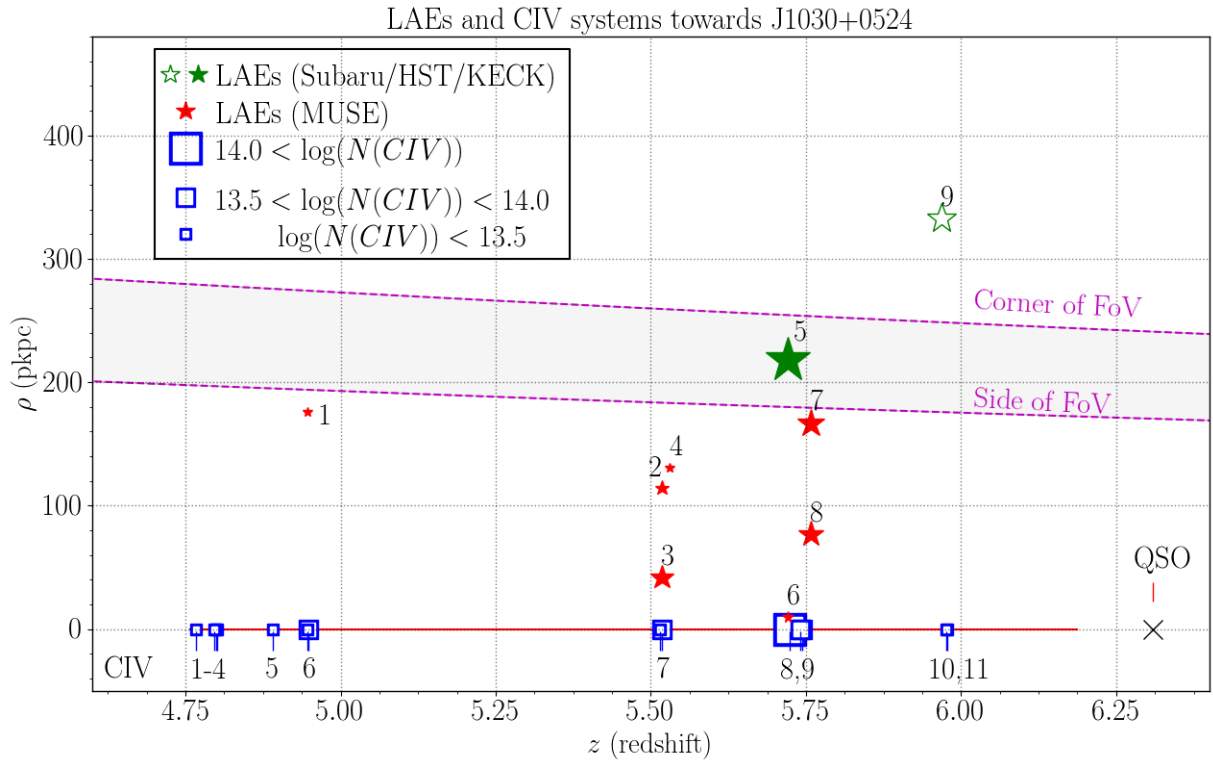


**Figure 14.** Representation of the spatial distribution of the LAEs respect to the C IV systems in J1030. The y-axis is the transverse distance in proper kpc and the x-axis is redshift. The QSO's redshift is indicated with an "X" and the absorption path is indicated with the red solid line at  $y = 0$ . Squares' sizes indicate the column density of the C IV absorption and the number is the ID from D'Odorico et al. (2013). Green star symbols are LAEs from our previous work, red star symbols are newly discovered LAEs. The size of the stars indicates the Ly $\alpha$  flux (see Tables 2 and 3). The FoV of MUSE (purple dashed line) shows the limit in transverse distance to search for C IV-galaxy associations imposed by the size of the FoV.

cles, respectively. In three cases, the closest LAEs are also within  $\pm 250 \text{ km s}^{-1}$  of the corresponding C IV. In the first case, C IV 6 is a double system with one LAE at 176 pkpc and almost the same redshift ( $\Delta V(\text{C IV} - \text{Ly}\alpha) = 71 \text{ km s}^{-1}$ ). The distance is not large enough to rule out a galactic wind scenario. Stepping forward in redshift, the double system C IV 7 at  $z_{\text{C IV}} = 5.5172$  has three associated LAEs: LAE #2, #3 and #4. The first two lie at less than  $\sim 2 \text{ km s}^{-1}$  from the absorption (second panel of Figure 15). In particular, the closest galaxy LAE #3 at 42 pkpc is also the brightest Ly $\alpha$  emission of the three. Moreover, the absorption system presents weak Si IV in both of the components. Similarly, C IV 8 at  $z_{\text{C IV}} = 5.72419$  has two associated LAEs at less than  $172 \text{ km s}^{-1}$ : LAE #5, which was previously reported in D'Áz et al. (2015) and remains the brightest

galaxy in the LAE sample of this work, and LAE #6, which is a new detection at  $\rho = 10 \text{ pkpc}$  to the C IV system. Figure 2 shows that LAE #5 and #6 are almost at opposite sides of the QSO's line-of-sight separated by  $\sim 223 \text{ pkpc}$  in projected distance, and  $\sim 50 \text{ km s}^{-1}$  in velocity. Thus it is not unreasonable to assume that these two galaxies are gravitationally bound, and that LAE #6 being the fainter of the two is a minor companion or satellite of LAE #5 (see section 5.1 for further discussion).

For the double system C IV 9 at  $z_{\text{C IV}} = 5.7428$  there are two confirmed LAEs at 167 pkpc (LAE #7) and at 77 pkpc (LAE #8), both at  $-639 \text{ km s}^{-1}$ . The asymmetry of the emission lines suggests that the true line centroids are bluer than our measurement thus the module of the velocity difference is only a lower limit in this

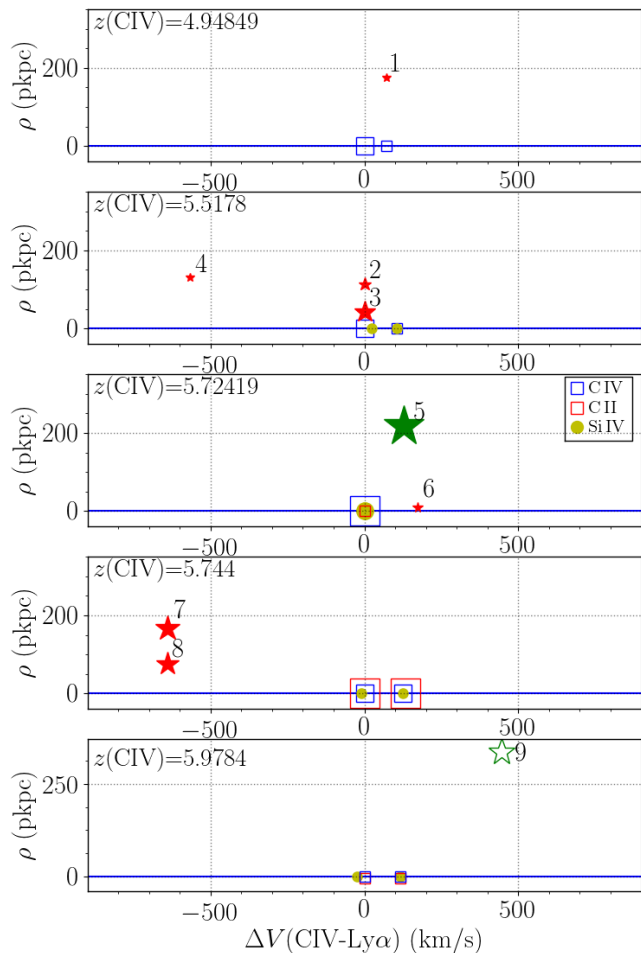


**Figure 15.** Impact parameter vs. radial velocity difference with the nearest C IV system. Three C IV systems have LAEs within  $\pm 250 \text{ km s}^{-1}$ . Note that all Ly $\alpha$  redshifts are measured from the blue edge of the Ly $\alpha$  profile, thus the systemic redshift of each galaxy is likely to be slightly lower than reported, resulting in positive (negative)  $\Delta V$  values likely being higher (lower) than reported. In the case of the LAEs at  $\approx -600 \text{ km s}^{-1}$ , the velocity difference would reduce. Using the empirical calibration developed by Verhamme et al. (2018), and typical FWHM velocities of  $200 \text{ km s}^{-1}$ , we expect each  $\Delta V$  value to be offset by  $140 \text{ km s}^{-1}$  to the right in the diagram above. Thus, all C IV systems have an LAE with a corrected redshift with  $500 \text{ km s}^{-1}$ .

case (the LAEs are likely closer). It is interesting to note that this particular system, with the largest velocity difference to the LAEs, is the only system with strong C II absorption (even higher column density than the C IV component).

Finally, the bottom panels of Figure 15 present the position of LAE 10 with respect to C IV 10 and 11. This LAE is clearly too far from the C IV to be the source of metals observed in absorption. However, the fact that two weak C IV systems with some evidence of Si IV have been found at less than  $\sim 530 \text{ km s}^{-1}$  is an indication that such C IV systems are associated with the environment of LAE 10, although the true sources of these absorptions are still to be found.

#### 4.5 C IV equivalent width and LAE impact parameter

Clear evidence of the existence of a chemically enriched CGM around star forming galaxies comes from the observed relation between  $W_0$  of absorption lines of different metals and the impact

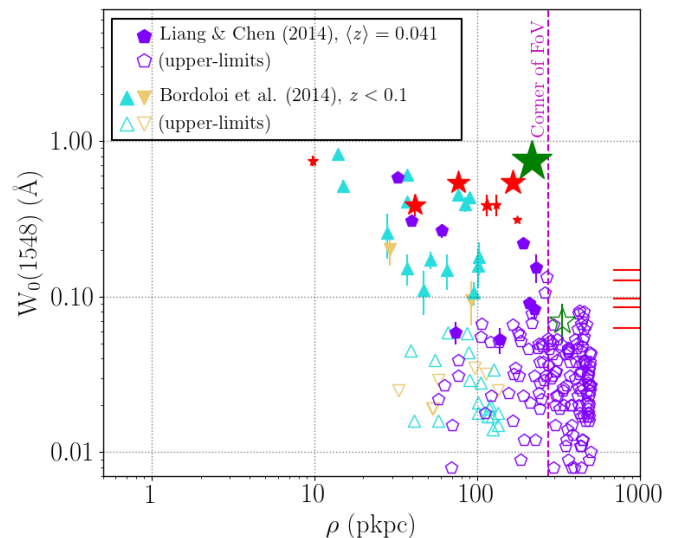


**Figure 16.** Rest-frame equivalent width of C IV versus impact parameter (transverse distance). Comparison with low mass (dwarf) local ( $z < 0.1$ ) galaxies from Liang & Chen (2014) (open and solid pentagons) and Bordoloi et al. (2014) (open and solid triangles). The vertical dashed line indicates the maximum distance from the center of the field of view (QSO's line of sight) to the corner. The horizontal line markers on the right side of each panel indicate the column density of four C IV systems from D'Odorico et al. (2013) for which we do not find a galaxy counterpart. The open circles indicate if the LAE is the closest detection to the corresponding C IV.

parameter ( $\rho$ ) to their closest neighbor galaxy (Adelberger et al. 2005; Steidel et al. 2010; Bouché et al. 2012). Figure 16 presents this relation for all the LAEs in this work (red star symbols) and provides a comparison with observations at  $z < 0.1$ .

We have found LAE counterparts of four of the five C IV systems with  $W_0(\text{C IV}) > 0.2 \text{ \AA}$ , within  $\rho \sim 270 \text{ kpc}$  (Figure 16). Regarding the six C IV systems with  $W_0(\text{C IV}) < 0.2 \text{ \AA}$ , none of them have a galaxy detection in MUSE's data-cube (horizontal red lines to the right of Figure 16), although two of them are neighbors of LAE #9 which is outside MUSE's FoV at  $\sim 335 \text{ pkpc}$ . Although the sample is small and affected by low number statistics, it seems that systems with  $W_0(\text{C IV}) > 0.2 \text{ \AA}$  at  $z = 5-6$  are likely to have galaxies with Ly $\alpha$  emission within  $\rho < 200 \text{ pkpc}$  (4/5 cases), whereas the C IV systems with  $W_0(\text{C IV}) < 0.2 \text{ \AA}$  do not seem to have a galaxy with detectable Ly $\alpha$  emission (0/6 cases). Therefore, *it is likely that the true sources of these weak absorption systems remain below the detection limit.*

#### 4.6 Ly $\alpha$ luminosity distribution

One of the most interesting results is the low Ly $\alpha$  luminosity of the candidates. Extensive efforts have been made in the past to study high-redshift galaxies in this field (Stiavelli et al. 2005; Kim et al. 2009; Morselli et al. 2014; Díaz et al. 2014, 2015; Cai et al. 2017). However, none of the previous studies reported the galaxies we detected with MUSE, except for LAE #5. The reason is that our LAEs are below the detection limits of recent works based on narrow-band and broad-band photometry (e.g. Santos et al. 2016; Konno et al. 2017). The top panel Figure 17 shows the luminosity function of  $z = 5.7$  LAEs from Santos et al. (2016), Konno et al. (2017) and Drake et al. (2017). The bottom plot presents the luminosity distribution of the LAEs from this work. Solid red histogram

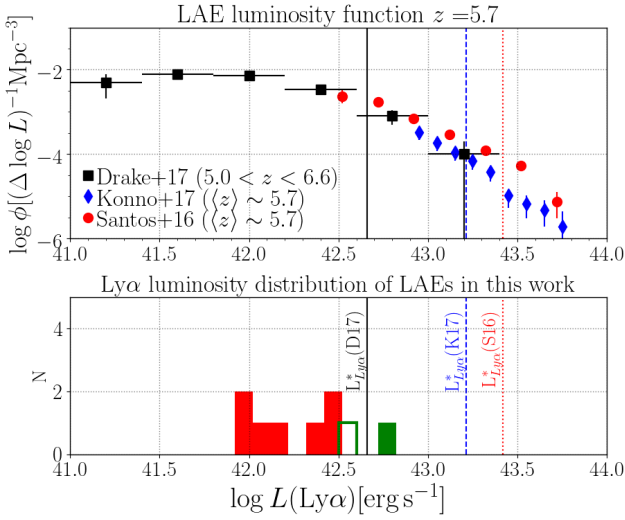


**Figure 17.** **Top:** Recent estimations of the luminosity function of LAEs at  $z = 5.7$  from Konno et al. (2017, blue squares) and Santos et al. (2016, red circles). **Bottom:** The distribution of the Ly $\alpha$  luminosity of LAEs in this work. The solid green bar represents LAE #5, the open green bar represents LAE #9 and the red histogram corresponds to the newly reported LAEs from MUSE’s data, showing that these type of galaxies are the population in the faint end of the most recent luminosity functions displayed in the top panel.

is for new detections with MUSE data, and green is for LAEs #5 and #9. We find that the LAEs in the environment of C iv systems trace the extrapolation of the faint end slope of the Ly $\alpha$  luminosity function, with some galaxies 0.5 dex fainter than the large LAE samples used by Santos et al. (2016) and Konno et al. (2017). In comparison with NB-selected samples, our candidates are in the range of  $L_{\text{Ly}\alpha} = 0.03\text{--}0.32 L_{\text{Ly}\alpha}^*$ , with  $\log(L_{\text{Ly}\alpha}^*) = 43.42$  (Santos et al. 2016) and  $\log(L_{\text{Ly}\alpha}^*) = 43.21$  (Konno et al. 2017).

The Ly $\alpha$  luminosity function measured with MUSE in the HUDF has probed the existence of LAEs that are even fainter than our sample, which are accessible only to wide-field IFUs. (Drake et al. 2017) reported  $\log(L_{\text{Ly}\alpha}^*) = 42.66$  based on 137 hours of MUSE observations covering  $3' \times 3'$  area. According to this new estimation, the luminosity of our sample is in the range  $L_{\text{Ly}\alpha} = 0.18\text{--}1.15 L_{\text{Ly}\alpha}^*$ , of which the only galaxy brighter than  $L_{\text{Ly}\alpha}^*$  is LAE #5 (solid green bar in Figure 17). In summary, the new sample of LAEs obtained with MUSE in the field of QSO J1030+0524 is fainter than  $L_{\text{Ly}\alpha}^*$ .

Finally, there is tentative evidence for a trend of fainter LAEs at smaller impact parameters. This is presented in the Ly $\alpha$  luminosity vs. impact parameter plot of Figure 18, which shows that LAEs at larger impact parameters are also more Ly $\alpha$  luminous. The circles indicate the LAEs with the smallest impact parameter for a given C iv system.

## 5 DISCUSSION

### 5.1 Faint optical galaxies polluting the IGM

The brightest LAE in the sample is LAE #5 ( $L_{\text{Ly}\alpha} = 1.15 L_{\text{Ly}\alpha}^*$ ), previously found at the same redshift of the C iv with the highest  $W_0$  of the sample. However, the impact parameter  $\rho \sim 218$  pkpc is in conflict with the outflow scenario for the origin of the absorption because, assuming formation at  $z = 30$ , a galaxy that has been

forming stars for less than  $\sim 900$  Myr would require high speed outflows to enrich such distances in a relatively short time (Díaz et al. 2015). The alternative scenario implies that the origin of the absorbing gas is a fainter (previously undetected) galaxy at a closer distance from the C iv system. García et al. (2017a) also concluded that the “dwarf satellite outflow” scenario is favored by state-of-the-art hydrodynamical simulations of the epoch of reionization. In this context, the detection of LAE #6 with  $L_{\text{Ly}\alpha} = 0.28 L_{\text{Ly}\alpha}^*$  at  $\rho = 10$  pkpc from the C iv, provides evidence for CGM-IGM chemical enrichment by satellites and neighbor dwarf galaxies at very early times, as predicted by computer simulations (e.g. Madau et al. 2001; Shen et al. 2012; García et al. 2017a).

The LAEs with smaller impact parameters to the C iv systems at  $z > 4.9$  are good candidates for the source of the metals because metal-enriched winds departing from the source at  $z = 10$  could have traversed this distance without the need for extreme outflow velocities. Figure 19 shows in blue dotted lines the distance that an outflow of mean speed  $\langle V_{\text{wind}} \rangle = 100, 200, 300$  and  $400 \text{ km s}^{-1}$  would cover if starting at  $z = 10$ . Except for LAE #1, the closest galaxies to the C iv systems are below the  $200 \text{ km s}^{-1}$  dotted line, which makes them good candidates for the sources of the metals.

The absence of LAE candidates within  $\rho = 200\text{--}250$  pkpc (i.e. inside MUSE’s FoV) of five C iv systems with  $W_0(\text{C iv}) < 0.2 \text{ \AA}$  is difficult to be explained by strong outflows from galaxies at  $\rho > 250$  pkpc (i.e. outside MUSE’s FoV). Given the short age of the Universe at these redshift, winds of several hundreds  $\text{km s}^{-1}$  must be active over most of the galaxy formation history to deliver metals at distances  $\rho > 250$  pkpc. For example, LAE #9 at  $\rho \sim 335$  pkpc is likely not the source of metals for C iv 10 and 11. One interpretation of this result is that there are galaxies below the detection limit of this work ( $2 \times 10^{-18} \text{ erg s}^{-1} \text{ cm}^{-2}$ ) which are probably close to the absorption systems.

It is possible that what we see at  $z > 4.75$  is the early contribution of low luminosity and low mass galaxies to the metal content of the CGM-IGM. Since mass estimates for the high- $z$  LAEs are not available, based on the mass-luminosity relation  $M_{\text{STAR}}/M_{\odot} - M_{\text{UV}}$  for  $z = 4\text{--}8$  UV-selected galaxies from Song et al. (2016) and the detection limit of  $M_{\text{UV}} < -20.5$  mag from Díaz et al. (2014), we estimate a conservative upper limit of  $\log(M_{\text{STAR}}/M_{\odot}) \lesssim 9.5$  for the newly reported LAEs in our sample (i.e. excluding LAE# 5 and LAE#9). For example, the range of Ly $\alpha$  luminosities of our LAEs  $L_{\text{Ly}\alpha} = 0.18\text{--}0.84 L_{\text{Ly}\alpha}^*$  has been associated to  $z > 3$  galaxies in the range  $\log(M_{\text{STAR}}/M_{\odot}) \lesssim 8.5$  (Karman et al. 2017). Although the physical properties of low-mass high- $z$  galaxies are under debate, several authors agree that these faint LAEs have typically very young ages, high specific star-formation rates, blue UV-continuum slope, low metallicities and low dust extinction (e.g. Trainor et al. 2016; Karman et al. 2017; Amorín et al. 2017; De Barros et al. 2017). Therefore, C iv systems at these redshifts could be tracing gas in the proximity of young and small galaxies, similar to the currently best candidates to drive the epoch of reionization at  $z > 6$  (Robertson et al. 2015; Atek et al. 2015; Castellano et al. 2016; Livermore et al. 2017).

### 5.2 Connection with UV background

The UV ionizing background radiation field (or UVB) became homogeneous at the Lyman limit rapidly after  $z \sim 5.5$ . During reionization and probably down to  $z \sim 5$ , the UVB was not spacially homogeneous (Fan et al. 2006; Becker et al. 2015b; Bosman et al. 2018; Eilers et al. 2018). Large spatial fluctuations are predicted

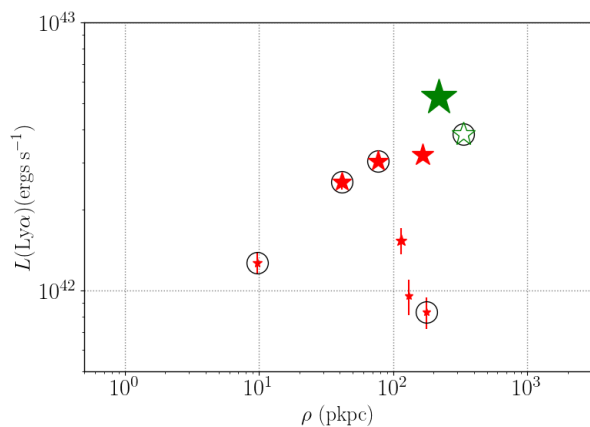


**Figure 18.** Luminosity of the Ly $\alpha$  emission as a function of impact parameter. The circles indicate the closest LAEs to the corresponding C IV system.

for the intensity and slope of this radiation, on scales of tens of comoving Mpc (Mesinger & Furlanetto 2009; Davies & Furlanetto 2016; Chardin et al. 2017; D’Aloisio et al. 2017; Keating et al. 2018; Upton Sanderbeck et al. 2019). Indeed, the discovery of one particularly long and opaque Ly $\alpha$  trough (Becker et al. 2015b) led to observations of a dearth of  $z \sim 5.7$  LAEs within 20  $h^{-1}$  comoving Mpc, confirming the prediction that the scatter in Ly $\alpha$  opacity is caused by spatical variation in the UVB over large scales (Becker et al. 2018). The Ly $\alpha$  opacity towards J1030+0524 has been measured by Eilers et al. (2018) at  $z=5.74$  to have an average flux of  $\langle F \rangle = 0.0144$ , which corresponds to a mean optical depth of  $\tau_{\text{eff}} = 4.2$ . We can use the mean surface density of LAEs in the field J1030+0524 within 10  $h^{-1}$  cMpc of  $0.107 \pm 0.004$  per square arcmin (Díaz et al. 2014) (noting this is a lower limit at a sensitivity of  $m_{\text{NB}}(5\sigma)=25.6$ ) to compare directly with Figure 14 in Davies et al. (2018). This middle-of-the-road Ly $\alpha$  opacity – Eilers et al. (2018) measures an average  $\tau_{\text{eff}} = 4.0057 \pm 0.2469$  at  $z = 5.75$ ) – has less leverage to test models which predict an associated under or over-density of galaxies. The measured opacity and galaxy density along this line of sight is consistent with both the fluctuating UVB (Davies et al. 2018) and fluctuating temperature models (D’Aloisio et al. 2017).

Such observations of Ly $\alpha$  opacity reflect the state of the UVB at 13.6 eV, whereas the energy required to ionize C III to C IV is 47.89 eV. Ideally, to probe the UVB at this energy, C IV itself should be used, this is somewhat complicated by the fact that C IV traces the metals around galaxies. Meyer et al. (2019) cross correlated 37 C IV systems at  $4.3 < z < 6.2$  with Ly $\alpha$  forest flux and found that the UVB is enhanced on scales greater than 10 cMpc (as measured by a decrease in forest absorption), whereas an excess of Ly $\alpha$  absorption is seen in the immediate vicinity of C IV systems. Furthermore most of the photons that ionize C III to C IV also have the energy to ionize He II. However, the Universe is optically-thin to He II only after  $z \sim 3$ . Therefore, the UVB relevant for C IV is highly inhomogeneous at  $z \sim 5.7$  despite H I reionization completing around  $z = 5 - 6$ . As a result, in the presence of an evolving ionizing background modulated by the environment, the detection of extended ionized metal halos around galaxies would also show a dependency with the ionizing properties of the local UVB.

The line of sight to J1030+0524 intercepts an excess of narrow-band selected LAEs at  $z = 5.7$ , and a deficit of broad-band selected LBGs, on scales of 10 cMpc with respect to the mean number den-

sity of galaxies on a  $80 \times 60$  cMpc FoV (Díaz et al. 2014). This was interpreted as an indication that an increase in C IV number density could be associated with a medium-density environment dominated by young star-forming galaxies on large scales. The current work presents evidence in support of the idea that strong C IV at  $z > 5.5$  is biased to highly ionized regions for the following reasons. We have found that the three systems at  $z > 5.5$  with  $W_0(\text{C IV}) > 0.5 \text{ \AA}$  and double C IV and Si IV components, have two or three LAEs within 200–220 pkpc. In addition, these galaxies are in the range  $L(\text{Ly}\alpha) = 0.18\text{--}1.15 L_{\text{Ly}\alpha}^*$ , mostly tracing the faint end of the Ly $\alpha$  luminosity function (Figure 17). These kind of LAEs have been found to have narrow line widths associated to low H I column densities (e.g. Guaita et al. 2017), strong optical emission lines associated to high ionization parameters (Nakajima & Ouchi 2014), extremely high nebular excitation (Trainor et al. 2016), and very high sSFR (Karman et al. 2017). Therefore, the narrow Ly $\alpha$  emission reveals the existence of recent star-formation under conditions that could favor the escape of ionizing radiation from the galaxy. Moreover, the thorough inspection of narrow band images from stacked frames described in section 3 did not returned any UV bright galaxy in MUSE’s FoV. This result supports previous conjectures that the C IV systems at the highest redshifts could be tracing a region of the Universe where large UV bright galaxies have not yet formed.

The surroundings of bright galaxies are guaranteed to be more enriched than the environment of faint galaxies because faint low-mass galaxies cluster around bright galaxies, and metallicity is predicted to increase monotonically with gas overdensity (e.g. Keating et al. 2016). As a consequence, the prevalence of C IV near faint LAEs would most likely be related to an overwhelming abundance of faint galaxies and/or their contribution to the local UVB rather than an generalized deficit of metals around bright galaxies.

In  $\Lambda$ CDM cosmology, the same faint dwarf galaxies that are expected to power reionization are also predicted to pollute the IGM/CGM with their heavy elements, which can be easily ejected outside these galaxies because of their shallow potential wells (e.g. Madau et al. 2001; Choudhury et al. 2008; Salvadori et al. 2014). Supernova-driven outflows inject metals into the CGM/IGM, heat gas that would otherwise fuel the next generation of star formation (keeping the galaxies faint) and may allow for the escape of a large fraction of Lyman continuum photons (e.g. Ferrara & Loeb 2013; Wise et al. 2014). A similar scenario has been proposed for the high- $z$  progenitors (satellites) of the Local Group (e.g. Salvadori et al. 2014), which at  $z \sim 5,6$  are predicted to be visible as faint LAEs ( $L(\text{Ly}\alpha) = 10^{39\text{--}43.25} \text{ erg s}^{-1}$  Salvadori et al. 2010). Therefore, their connection to high-ionization absorption systems is potentially a consequence of the role of satellites in the early evolution of the CGM and the IGM.

The potential of faint galaxies boosting the local UVB at  $z \sim 5.75$  is suggested by the latest results from the cosmological hydrodynamic Technicolor Dawn simulations. (Finlator et al. 2020) explore the environment of strong C IV systems at  $z > 5$  and reports that a density-bounded escape fraction model which hardens the emerging flux from galaxies, results in an ionizing background that produces the observed volume-averaged hydrogen ionization rate while boosting the predicted C IV abundance into better agreement with observations than previous models. In addition, they predict that galaxies and strong C IV systems are positively correlated out to  $\sim 300$  proper kpc, with  $\sim 2$  faint LAEs ( $\log(L_{\text{Ly}\alpha}) > 40.8$ ) within 100 pkpc at  $z = 5.75$ . Our results are in total agreement with this predictions: although we do not reach the Ly $\alpha$  luminosity limit of  $\log(L_{\text{Ly}\alpha}) > 40.8$ , we have found multiple LAEs within  $\sim 250$

pkpc of three strong C IV systems ( $W_0 > 0.2\text{\AA}$ ) at  $z > 5.5$ , with the faintest examples lying at  $\rho < 100$  pkpc.

If the common assumption that LyC photons are easier to escape from low mass galaxies is confirmed (e.g. [Bian et al. 2017](#)), low luminosity LAEs would be a very common source of ionizing photons at high- $z$ . Therefore, having found several low luminosity LAEs among the highest redshift C IV, it is possible that such absorption systems are sensitive to the local conditions of the ionizing background provided by the LAEs. In this case, the highly ionized surroundings of these particular galaxies would have facilitated the detection of C IV in the CGM. This opens the possibility that C IV systems at  $z \gtrsim 5.5$  could have a preference for recently ionized environments, which should be tested with larger samples and observations of similar or better depth.

In summary, although the Ly $\alpha$  opacity of this line of sight is average, the galaxy environment along this C IV-rich line of sight is characterized by an enhanced number density of faint LAEs near strong C IV, and a lack of UV-bright counterparts for 11 C IV systems. This excess of faint galaxies could boost the UVB at energies higher than 1 Rydberg. Many more line of sight are required to test the connection between Ly $\alpha$  opacity, C IV absorbers and galaxies at  $z > 5.5$ .

### 5.3 The size of the metal enriched CGM

The distribution of individual LAEs near C IV systems at  $z = 4.95$ – $5.97$  shows a tentative decrease in  $W_0(\text{C IV})$  with increasing  $\rho$  and there is no evidence for a significant drop at  $\rho < 200$ . The accumulation of metals in the CGM over time, driven by star-formation and outflows from the central galaxy and its satellites, leads to a natural growth in  $W_0$  of the absorption systems observed near the galaxies. Therefore, the maximum of the distribution of galaxies in the  $\rho$  vs.  $W_0(\text{C IV})$  plane (Figure 16) would increase with time (larger  $W_0$  at lower redshift) and with halo mass, which is supported by the observations of the mean C IV distribution around bright LBGs at  $z \sim 2.2$ – $2.4$  ([Steidel et al. 2010](#)). However, the evolution with time of the maximum detectable distance (i.e. the size of the C IV “bubble”), might depend on the efficiency of the feedback mechanisms driving outflows and the energy distribution of the UVB radiation.

The source of weak C IV absorbing clouds for which no LAE candidate was detected, could be a Ly $\alpha$  emitters below our detections limit, or could have stopped emitting Ly $\alpha$  photons, or the Ly $\alpha$  emission is absorbed by intervening Lyman Limit Systems or Damped Lyman Alpha systems (which are more common at higher redshifts). These alternatives have in common that the source would be an object in the low-mass regime, implying outflows with average low speeds and/or short travel times that result in a low covering fraction of ionized metals. These would make the C IV absorption detectable only at small impact parameters from the source. Therefore, the missing sources are likely to be close (within a few tens of kpc) to the absorbing gas. These faint galaxies are only accessible to current capabilities through very deep observations (e.g.  $> 10$  hours with MUSE, [Drake et al. 2017](#)) or through gravitational lensing (e.g. [Karman et al. 2017](#)).

However, studies of low redshift galaxies using background QSOs have demonstrated the high incidence of C IV in the CGM of low luminosity and low mass galaxies. For example, the 43 galaxies in the COS-Dwarfs program revealed that C IV is detected out to  $\sim 100$  pkpc in dwarf galaxies at  $z < 0.1$  ([Bordoloi et al. 2014](#)). The C IV in the CGM of these faint galaxies could account for  $\sim 60\%$  of the  $W_0(1548) > 0.1\text{\AA}$  absorptions at low- $z$ . [Liang & Chen \(2014\)](#) study the low- and high-ionization metal transitions in the CGM

of 195 isolated galaxies at  $\langle z \rangle = 0.041$  over a wide stellar mass range. They find a large contribution of dwarf galaxies to the C IV content of the CGM, and a general absence of heavy elements at  $\rho > 0.7R_h$  (where  $R_h$  is the dark matter halo radius). Figure 16 shows that the distribution of high- $z$  LAEs and C IV systems in the  $W_0$  vs.  $\rho$  plane<sup>3</sup> is in good agreement with the low redshift samples of sub-L\* galaxies at  $z \lesssim 0.1$  from [Bordoloi et al. \(2014\)](#) and [Liang & Chen \(2014\)](#). If C IV absorptions at  $z > 5$  and  $z < 0.1$  trace the CGM of dwarf galaxies in low-density environments, it is worth to consider the possibility to search for local analogs of reionization epoch galaxies based on low mass galaxies with high column density of photoionized gas in the CGM. In order to obtain a truly unbiased view of the evolution of the CGM, the comparison of galaxies near C IV detections at different redshifts requires a blind survey of galaxies in fields with detected metals absorption systems.

### 5.4 Implications for chemical enrichment

Our findings that C IV systems are in regions with more than one sub-L\*<sub>Ly $\alpha$</sub>  LAE, is an indication that C IV systems are tracing environments of recent star-formation. This result has important implications for the chemical enrichment of the Universe. As we look back in time, the mean metallicity of the Universe decreases predictably as a function of the star formation rate density, moderated by the yield and return fraction of metals ([Madau & Dickinson 2014](#)). Ideally, our observations would capture a full census of all ions, but in practice they are limited to those with favourable transitions. The evolution of the comoving mass density of C IV,  $\Omega_{\text{C IV}}$ , reflects both the metallicity of intervening IGM and CGM absorbers as well as the fraction of Carbon in the triply ionized state. The value of  $\Omega_{\text{C IV}}$  declines mildly over the 12.5 billion years from redshift  $z \sim 0$  to  $z \sim 5$  ([Songaila 2001](#); [Scannapieco et al. 2006](#); [Danforth & Shull 2008](#); [Cooksey et al. 2010, 2013](#); [D’Odorico et al. 2010](#); [Boksenberg & Sargent 2015](#)). In contrast,  $\Omega_{\text{C IV}}$  appear to decline considerably over a much shorter period of time, 300 million years, from redshift 5 to 6 ([Ryan-Weber et al. 2009](#); [Becker et al. 2009](#); [Simcoe et al. 2011](#); [D’Odorico et al. 2013](#); [Díaz et al. 2016](#); [Codoreanu et al. 2018](#); [Meyer et al. 2019](#)). Despite considerable observational effort to determine this drop in  $\Omega_{\text{C IV}}$ , the exact factor decrease is not well measured. This is due to low number statistics of C IV absorbers at  $z \sim 6$  together with differences in resolution and sensitivity across different studies. Interestingly, this drop in C IV seems to be balanced with a rise in C II ([Cooper et al. 2019](#)).

The decline in the number of C IV absorbers with redshift has been attributed to a combination of a decrease in metallicity –the metal content of the CGM-IGM– towards higher redshift and a decrease in the intensity of the background ionizing flux that such metals are exposed to. This change could be caused by a reduction, towards larger redshift, in the number of sources with detectable C IV systems and/or a change in the covering fraction of the absorbing gas. Both effects are probably in place. In the first case, the number of sources with detectable C IV would decrease because high ionization regions are less uniform and less common towards the epoch of reionization. In the second case, the association to young galaxies implies recent star formation, thus outflows are in their early stages and will produce streams of baryons with a small projected area on the sky.

Models support both interpretations: [Finlator et al. \(2015\)](#) cite a

<sup>3</sup> Values reported in the literature only include the equivalent width of the stronger line component of the C IV doublet at 1548 Å.

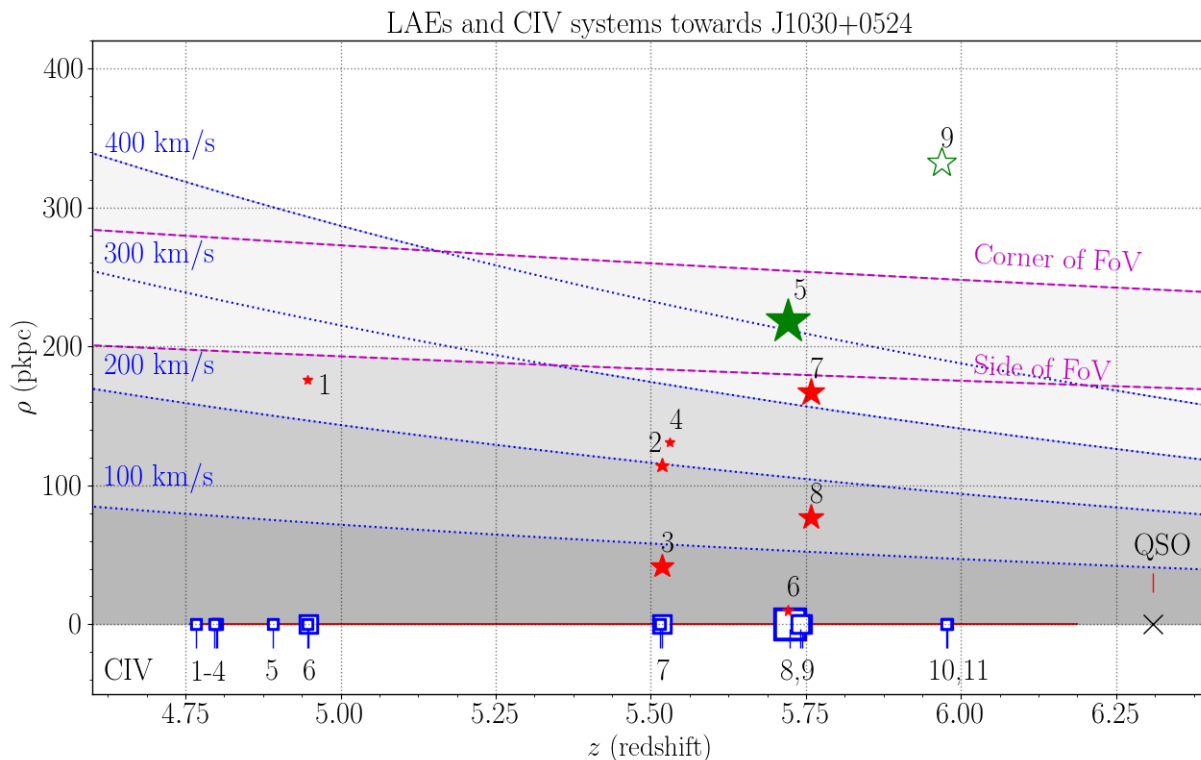


**Figure 19.** Reproduction of Figure 14 with shaded areas indicating the distance reached by an outflow starting at  $z = 10$  and mean speed  $\langle V_{wind} \rangle = 100, 200, 300$  and  $400 \text{ km s}^{-1}$ .

combination of ongoing enrichment and ionization in roughly equal measure. By examining the evolution of low ionization systems the degeneracy between metallicity and UVB can be broken. Hints of an increase in the number of low equivalent width Mg II systems is seen around a redshift of 5 (Bosman et al. 2017; Chen et al. 2017; Codoreanu et al. 2017). Evidence of the effect on the softening of the UVB on CGM scales has been recently demonstrated by O I absorption lines showing a significant upturn in their number density at  $z > 5.7$  (Becker et al. 2019).

Although these arguments need to be tested with larger samples, our findings of faint galaxies in close proximity to C IV systems at  $z > 5$  suggest that the absorbing material was ejected in the recent past. Figure 19 shows that for C IV systems 7, 8 and 9, the LAEs are within the reach of outflows of  $\langle v \rangle \sim 100\text{--}150 \text{ km s}^{-1}$  starting at  $z = 10$ . This is evidence that we are witnessing the first ejection of metals to the CGM-IGM, which would indicate that one of the reasons of the drop in  $\Omega_{CIV}$  is a decrease in the amount of metals outside of galaxies, reflected in the covering fraction.

## 6 CONCLUSION

We conducted a search for LAEs in the line of sight to QSO J1030+0524, using MUSE at VLT, to identify the galaxies within  $\lesssim 250 \text{ pkpc}$  (transversal distance) from of 11 C IV absorption systems in the redshift range  $z = 4.76\text{--}5.97$ . The results can be summarized as follows:

- We report the detection of at least one LAE in close proximity to the four C IV systems with  $\log_{10}(N_{CIV}[\text{cm}^{-2}]) > 13.5$  and multiple LAEs for the systems at  $z_{CIV} > 5.5$ . The closest LAEs are

also within  $\pm 250 \text{ km s}^{-1}$  from the corresponding C IV. The exception are LAE #7 and #8 at  $-639 \text{ km s}^{-1}$  from C IV 9. In contrast, we find no LAE within  $\rho < 200\text{--}250 \text{ pkpc}$  of the seven weaker C IV systems ( $\log_{10}(N_{CIV}[\text{cm}^{-2}]) < 13.5$ ), although two of them have one LAE neighbor at  $335 \text{ pkpc}$ . Overall, C IV systems with  $\log_{10}(N_{CIV}[\text{cm}^{-2}]) > 13.5$  at  $z = 5\text{--}6$  are more likely to have galaxies with Ly $\alpha$  emission within  $\rho < 200 \text{ pkpc}$  (4/4 cases) than the C IV systems with  $\log_{10}(N_{CIV}[\text{cm}^{-2}]) < 13.5$  (0/7 cases).

- The absence of LAE candidates for seven C IV systems with  $\log_{10}(N_{CIV}[\text{cm}^{-2}]) < 13.5$  is difficult to be explained by strong outflows from galaxies at  $\rho > 200 \text{ pkpc}$  (outside MUSE’s FoV). We conclude that the true sources of weak C IV absorbing clouds remain below the detection limit of this work ( $2 \times 10^{-18} \text{ erg s}^{-1} \text{ cm}^{-2}$ ) because their Ly $\alpha$  luminosity is simply too low, or they have stopped emitting Ly $\alpha$  photons, or the emission is absorbed by intervening neutral hydrogen (LLSs, DLAs, etc).

- We present LAE #6, which is a  $0.28 L_{Ly\alpha}^*$  galaxy at  $\rho = 10 \text{ pkpc}$  from the strongest C IV, and represents the first clear example of enrichment by satellites and neighbor dwarf galaxies at very early times. LAE #5 is the brightest LAE in the sample ( $1.15 L_{Ly\alpha}^*$ ) which was detected with standard broad-band images by Díaz et al. (2014). LAE #5 and LAE #6 are detected at opposite sides of the QSO’s line-of-sight separated by  $\sim 140 \text{ pkpc}$  in projected distance, and  $\sim 50 \text{ km s}^{-1}$  in velocity. Thus, the two galaxies could be gravitationally bound. This is observational evidence that supports the prediction from hydrodynamical simulations that low-mass satellites drive the CGM-IGM enrichment at very early times (e.g. Garca et al. 2017a).

- The comparison of the  $W_0$  vs.  $\rho$  of individual galaxies shows that the C IV in absorption at  $z > 4.94$  in the sight-line of this study is similar to the CGM of low- $z$  dwarf galaxies in low-density



environments. This is another indication that the systems at  $z > 4.94$  are tracing the early contribution of low luminosity and low mass galaxies to the metal content of the CGM-IGM.

- We find that the environment of C IV systems within 200 pkpc is populated by the faint end of the Ly $\alpha$  luminosity function with some galaxies reaching luminosities fainter than  $0.2 L^*(\text{Ly}\alpha)$  (0.5 dex fainter than those currently used to determine the luminosity function) and  $M_{\text{UV}} < -20.5$  mag. This is an indication that C IV at these redshifts are tracing gas in the proximities of young and small galaxies, similar to the currently best candidates to drive the epoch of reionization at  $z > 6$ .

- The detection of several low luminosity LAEs among the highest redshift C IV, and the lack of bright counterparts for 11 C IV systems could indicate a connection between environment and the ionization state of the CGM-IGM. For example, if C IV systems at  $z \gtrsim 5.5$  are sensitive to the local ionizing conditions provided by the LAEs, it might be possible to use C IV systems to trace similar regions at higher redshift in the search for highly ionizing sources.

- Our findings of faint galaxies in close proximity to C IV systems at  $z > 5$  suggest that the absorbing material was ejected in the recent past. Figure 19 shows that, except for LAE #1, all the closest pairs are below the  $200 \text{ km s}^{-1}$  dotted line. Also, for C IV systems 7, 8 and 9, the LAE counterpart is within the reach of outflows of  $\langle v \rangle \sim 100\text{--}150 \text{ km s}^{-1}$  starting at  $z = 10$ .

The connection between faint star-forming galaxies and high-ionization absorption systems reported in this work, is potentially a consequence of the role of satellites in the early evolution of the CGM and the IGM. Assuming that faint LAEs are mainly young star-forming galaxies, the detection of these galaxies near strong C IV systems supports the scenario in which the decrease in the C IV comoving mass density  $\Omega_{\text{C IV}}$  and the column density distribution function of C IV towards  $z > 5.3$  is a combination of: a) low covering fraction due to a decrease in the amount of metals outside of galaxies, and b) a bias with environment possibly driven by the effect of local ionizing sources in the UVB.

The mechanical feedback of outflows required to eject metals to the CGM-IGM, might also have an impact on the reionization of hydrogen in the IGM by pouring holes in the star-forming regions which allow the escape of ionizing (Lyman continuum) photons. As a result, the same internal processes that would connect LAEs and C IV systems would also provide the means for the escape of ionizing photons. In this picture, the same faint low-mass galaxies providers of metals to the high- $z$  IGM are also important sources of ionizing photons.

Finally, this work clearly demonstrates the key role of large integral field units like MUSE in the search for very faint emission line galaxies. The MUSE Hubble Ultra Deep Field Survey has demonstrated the detection of low luminosity galaxies whose only signature is a faint Ly $\alpha$  emission line, that is, no continuum is detected, including in deep HST images (see e.g. Hashimoto et al. 2017). JWST will not capture these faint Lyman-alpha emitting galaxies with its imaging surveys and ground-based spectroscopy can only follow-up the space-based detections. Our data demonstrates that the Ly $\alpha$  emission of the faintest galaxies is only a few Angstrom wide, which is less than one pixel of the JWST NIRCам GRISM (1 nm/pixel). However, MUSE wavelength coverage ends at 930nm corresponding to Ly $\alpha$   $z \sim 6.6$ . Proposed future instruments such as the Keck Cosmic Reionization Mapper (KCRM) will continue to 1050nm (Ly $\alpha$  at  $z = 7.6$ ). This will allow the detection of faint Lyman-alpha emitting galaxies between redshift 6.6 and 7.6 which is critical to understanding the reionization of the Uni-

verse by (1) measuring the attenuation of Ly $\alpha$  emission equivalent width with respect to the underlying UV continuum (e.g. Furusawa et al. 2016) and (2) a census of the galaxies most likely to have the largest contribution to the UV radiation that reionized the Universe at  $z > 6$ .

## ACKNOWLEDGEMENTS

CGD would like to thank Kristian Finlator for all the interesting discussions that helped improving this work. CGD acknowledges the support of the Consejo de Investigaciones Científicas y Técnicas (CONICET) and the Gemini Observatory. ERW acknowledges that parts of this research were conducted by the Australian Research Council Centre of Excellence for All Sky Astrophysics in 3 Dimensions (ASTRO 3D), through project number CE170100013. KIC acknowledges funding from the European Research Council through the award of the Consolidator Grant ID 681627-BUILDUP. SS acknowledges support from the ERC Starting Grant NEFERITTI H2020/804240.

## REFERENCES

- Adelberger K. L., Shapley A. E., Steidel C. C., Pettini M., Erb D. K., Reddy N. A., 2005, *ApJ*, 629, 636
- Amorín R., et al., 2017, *Nature Astronomy*, 1, 0052
- Atek H., et al., 2015, *ApJ*, 814, 69
- Bacon R., et al., 2012, *The Messenger*, 147, 4
- Bacon R., Piqueras L., Conseil S., Richard J., Shepherd M., 2016, MPA&F: MUSE Python Data Analysis Framework, Astrophysics Source Code Library (ascl:1611.003)
- Becker G. D., Rauch M., Sargent W. L. W., 2009, *ApJ*, 698, 1010
- Becker G. D., Bolton J. S., Lidz A., 2015a, *Publ. Astron. Soc. Australia*, 32, e045
- Becker G. D., Bolton J. S., Madau P., Pettini M., Ryan-Weber E. V., Venemans B. P., 2015b, *MNRAS*, 447, 3402
- Becker G. D., Davies F. B., Furlanetto S. R., Malkan M. A., Boera E., Douglass C., 2018, *ApJ*, 863, 92
- Becker G. D., et al., 2019, *ApJ*, 883, 163
- Bertin E., Arnouts S., 1996, *A&AS*, 117, 393
- Bian F., Fan X., McGreer I., Cai Z., Jiang L., 2017, *ApJ*, 837, L12
- Boksenberg A., Sargent W. L. W., 2015, *ApJS*, 218, 7
- Bordoloi R., et al., 2014, *ApJ*, 796, 136
- Borthakur S., et al., 2015, *ApJ*, 813, 46
- Bosman S. E. I., Becker G. D., Haehnelt M. G., Hewett P. C., McMahon R. G., Mortlock D. J., Simpson C., Venemans B. P., 2017, *MNRAS*, 470, 1919
- Bosman S. E. I., Fan X., Jiang L., Reed S., Matsuoka Y., Becker G., Haehnelt M., 2018, *MNRAS*, 479, 1055
- Bouché N., Hohensee W., Vargas R., Kacprzak G. G., Martin C. L., Cooke J., Churchill C. W., 2012, *MNRAS*, 426, 801
- Bowen D. V., Chelouche D., Jenkins E. B., Tripp T. M., Pettini M., York D. G., Frye B. L., 2016, *ApJ*, 826, 50
- Bradshaw E. J., et al., 2013, *MNRAS*, 433, 194
- Burchett J. N., Tripp T. M., Werk J. K., Howk J. C., Prochaska J. X., Ford A. B., Davé R., 2013, *ApJ*, 779, L17
- Burchett J. N., et al., 2015, *ApJ*, 815, 91
- Burchett J. N., et al., 2016, *ApJ*, 832, 124
- Cai Z., Fan X., Dave R., Finlator K., Oppenheimer B., 2017, *ApJ*, 849, L18
- Castellano M., et al., 2016, *ApJ*, 818, L3
- Cen R., Chisari N. E., 2011, *ApJ*, 731, 11
- Chardin J., Puchwein E., Haehnelt M. G., 2017, *MNRAS*, 465, 3429
- Chen H.-W., Lanzetta K. M., Webb J. K., 2001, *ApJ*, 556, 158
- Chen S.-F. S., et al., 2017, *ApJ*, 850, 188
- Choudhury T. R., Ferrara A., Gallerani S., 2008, *MNRAS*, 385, L58

- Codoreanu A., Ryan-Weber E. V., Crighton N. H. M., Becker G., Pettini M., Madau P., Venemans B., 2017, *MNRAS*, **472**, 1023
- Codoreanu A., Ryan-Weber E. V., García L. Á., Crighton N. H. M., Becker G., Pettini M., Madau P., Venemans B., 2018, *MNRAS*, **481**, 4940
- Cooksey K. L., Thom C., Prochaska J. X., Chen H.-W., 2010, *ApJ*, **708**, 868
- Cooksey K. L., Kao M. M., Simcoe R. A., O’Meara J. M., Prochaska J. X., 2013, *ApJ*, **763**, 37
- Cooper T. J., Simcoe R. A., Cooksey K. L., Bordoloi R., Miller D. R., Furesz G., Turner M. L., Bañados E., 2019, *ApJ*, **882**, 77
- D’Aloisio A., Upton Sanderbeck P. R., McQuinn M., Trac H., Shapiro P. R., 2017, *MNRAS*, **468**, 4691
- D’Odorico V., Calura F., Cristiani S., Viel M., 2010, *MNRAS*, **401**, 2715
- D’Odorico V., et al., 2013, *MNRAS*, **435**, 1198
- Danforth C. W., Shull J. M., 2008, *ApJ*, **679**, 194
- Davé R., Finlator K., Oppenheimer B. D., 2011, *MNRAS*, **416**, 1354
- Davies F. B., Furlanetto S. R., 2016, *MNRAS*, **460**, 1328
- Davies F. B., Becker G. D., Furlanetto S. R., 2018, *ApJ*, **860**, 155
- De Barros S., et al., 2017, *A&A*, **608**, A123
- Dekel A., et al., 2009, *Nature*, **457**, 451
- Díaz C. G., Ryan-Weber E. V., Cooke J., Pettini M., Madau P., 2011, *MNRAS*, **418**, 820
- Díaz C. G., Koyama Y., Ryan-Weber E. V., Cooke J., Ouchi M., Shimasaku K., Nakata F., 2014, *MNRAS*, **442**, 946
- Díaz C. G., Ryan-Weber E. V., Cooke J., Koyama Y., Ouchi M., 2015, *MNRAS*, **448**, 1240
- Díaz C. G., Ryan-Weber E. V., Codoreanu A., Pettini M., Madau P., 2016, *Boletín de la Asociación Argentina de Astronomía La Plata Argentina*, **58**, 54
- Drake A. B., et al., 2017, *A&A*, **608**, A6
- Eilers A.-C., Davies F. B., Hennawi J. F., 2018, *ApJ*, **864**, 53
- Fan X., et al., 2006, *AJ*, **132**, 117
- Ferrara A., Loeb A., 2013, *MNRAS*, **431**, 2826
- Ferrara A., Scannapieco E., Bergeron J., 2005, *ApJ*, **634**, L37
- Finlator K., Thompson R., Huang S., Davé R., Zackrisson E., Oppenheimer B. D., 2015, *MNRAS*, **447**, 2526
- Finlator K., Oppenheimer B. D., Davé R., Zackrisson E., Thompson R., Huang S., 2016, *MNRAS*, **459**, 2299
- Finlator K., Doughty C., Cai Z., Díaz G., 2020, arXiv e-prints, [p. arXiv:2001.03498](https://arxiv.org/abs/2001.03498)
- Fontanot F., Hirschmann M., De Lucia G., 2017, *ApJ*, **842**, L14
- Ford A. B., Davé R., Oppenheimer B. D., Katz N., Kollmeier J. A., Thompson R., Weinberg D. H., 2014, *MNRAS*, **444**, 1260
- Furusawa H., et al., 2016, *ApJ*, **822**, 46
- García L. A., Tescari E., Ryan-Weber E. V., Wyithe J. S. B., 2017a, *MNRAS*, **469**, L53
- García L. A., Tescari E., Ryan-Weber E. V., Wyithe J. S. B., 2017b, *MNRAS*, **470**, 2494
- Guaita L., et al., 2017, *A&A*, **606**, A19
- Hashimoto T., Ouchi M., Shimasaku K., Ono Y., Nakajima K., Rauch M., Lee J., Okamura S., 2013, *ApJ*, **775**, 140
- Hashimoto T., et al., 2017, *A&A*, **608**, A10
- Ho S. H., Martin C. L., Kacprzak G. G., Churchill C. W., 2017, *ApJ*, **835**, 267
- Hopkins P. F., Quataert E., Murray N., 2012, *MNRAS*, **421**, 3522
- Hopkins P. F., Kereš D., Oñorbe J., Faucher-Giguère C.-A., Quataert E., Murray N., Bullock J. S., 2014, *MNRAS*, **445**, 581
- Karman W., Caputi K. I., Trager S. C., Almaini O., Cirasuolo M., 2014, *A&A*, **565**, A5
- Karman W., et al., 2015, *A&A*, **574**, A11
- Karman W., et al., 2017, *A&A*, **599**, A28
- Kashikawa N., et al., 2006, *ApJ*, **648**, 7
- Keating L. C., Puchwein E., Haehnelt M. G., Bird S., Bolton J. S., 2016, *MNRAS*, **461**, 606
- Keating L. C., Puchwein E., Haehnelt M. G., 2018, *MNRAS*, **477**, 5501
- Kereš D., Katz N., Weinberg D. H., Davé R., 2005, *MNRAS*, **363**, 2
- Kim S., et al., 2009, *ApJ*, **695**, 809
- Konno A., et al., 2017, *PASJ*,
- Lehner N., O’Meara J. M., Fox A. J., Howk J. C., Prochaska J. X., Burns V., Armstrong A. A., 2014, *ApJ*, **788**, 119
- Liang C. J., Chen H.-W., 2014, *MNRAS*, **445**, 2061
- Livermore R. C., Finkelstein S. L., Lotz J. M., 2017, *ApJ*, **835**, 113
- Madau P., Dickinson M., 2014, *ARA&A*, **52**, 415
- Madau P., Ferrara A., Rees M. J., 2001, *ApJ*, **555**, 92
- Mesinger A., Furlanetto S., 2009, *MNRAS*, **400**, 1461
- Meyer R. A., Bosman S. E. I., Kakiichi K., Ellis R. S., 2019, *MNRAS*, **483**, 19
- Morselli L., et al., 2014, *A&A*, **568**, A1
- Muratov A. L., Kereš D., Faucher-Giguère C.-A., Hopkins P. F., Quataert E., Murray N., 2015, *MNRAS*, **454**, 2691
- Nakajima K., Ouchi M., 2014, *MNRAS*, **442**, 900
- Nielsen N. M., Churchill C. W., Kacprzak G. G., 2013, *ApJ*, **776**, 115
- Oppenheimer B. D., Davé R., 2008, *MNRAS*, **387**, 577
- Oppenheimer B. D., Davé R., Finlator K., 2009, *MNRAS*, **396**, 729
- Oppenheimer B. D., Davé R., Kereš D., Fardal M., Katz N., Kollmeier J. A., Weinberg D. H., 2010, *MNRAS*, **406**, 2325
- Pallottini A., Ferrara A., Gallerani S., Salvadori S., D’Odorico V., 2014, *MNRAS*, **440**, 2498
- Peeples M. S., Werk J. K., Tumlinson J., Oppenheimer B. D., Prochaska J. X., Katz N., Weinberg D. H., 2014, *ApJ*, **786**, 54
- Persic M., Salucci P., 1992, *MNRAS*, **258**, 14P
- Pettini M., Shapley A. E., Steidel C. C., Cuby J.-G., Dickinson M., Moorwood A. F. M., Adelberger K. L., Giallisco M., 2001, *ApJ*, **554**, 981
- Planck Collaboration et al., 2014, *A&A*, **571**, A16
- Prochaska J. X., Weiner B., Chen H.-W., Mulchaey J., Cooksey K., 2011, *ApJ*, **740**, 91
- Rahmati A., Schaye J., Crain R. A., Oppenheimer B. D., Schaller M., Theuns T., 2016, *MNRAS*, **459**, 310
- Revaz Y., Jablonka P., 2018, preprint, ([arXiv:1801.06222](https://arxiv.org/abs/1801.06222))
- Robertson B. E., Ellis R. S., Furlanetto S. R., Dunlop J. S., 2015, *ApJ*, **802**, L19
- Rubin K. H. R., Prochaska J. X., Koo D. C., Phillips A. C., 2012, *ApJ*, **747**, L26
- Rubin K. H. R., Prochaska J. X., Koo D. C., Phillips A. C., Martin C. L., Winstrom L. O., 2014, *ApJ*, **794**, 156
- Ryan-Weber E. V., Pettini M., Madau P., 2006, *MNRAS*, **371**, L78
- Ryan-Weber E. V., Pettini M., Madau P., Zych B. J., 2009, *MNRAS*, **395**, 1476
- Salvadori S., Dayal P., Ferrara A., 2010, *MNRAS*, **407**, L1
- Salvadori S., Tolstoy E., Ferrara A., Zaroubi S., 2014, *MNRAS*, **437**, L26
- Salvadori S., Skúladóttir Á., Tolstoy E., 2015, *MNRAS*, **454**, 1320
- Santos S., Sobral D., Matthee J., 2016, *MNRAS*, **463**, 1678
- Scannapieco E., Pichon C., Aracil B., Petitjean P., Thacker R. J., Pogosyan D., Bergeron J., Couchman H. M. P., 2006, *MNRAS*, **365**, 615
- Shapley A. E., Steidel C. C., Pettini M., Adelberger K. L., 2003, *ApJ*, **588**, 65
- Shen S., Madau P., Aguirre A., Guedes J., Mayer L., Wadsley J., 2012, *ApJ*, **760**, 50
- Shull J. M., Smith B. D., Danforth C. W., 2012, *ApJ*, **759**, 23
- Simcoe R. A., et al., 2011, *ApJ*, **743**, 21
- Somerville R. S., Davé R., 2015, *ARA&A*, **53**, 51
- Song M., et al., 2016, *ApJ*, **825**, 5
- Songaila A., 2001, *ApJ*, **561**, L153
- Steidel C. C., Erb D. K., Shapley A. E., Pettini M., Reddy N., Bogosavljević M., Rudie G. C., Rakic O., 2010, *ApJ*, **717**, 289
- Stiavelli M., et al., 2005, *ApJ*, **622**, L1
- Stocke J. T., Keeney B. A., Danforth C. W., Shull J. M., Froning C. S., Green J. C., Penton S. V., Savage B. D., 2013, *ApJ*, **763**, 148
- Tejos N., et al., 2014, *MNRAS*, **437**, 2017
- Tescari E., Viel M., D’Odorico V., Cristiani S., Calura F., Borgani S., Tornatore L., 2011, *MNRAS*, **411**, 826
- Trainor R. F., Strom A. L., Steidel C. C., Rudie G. C., 2016, *ApJ*, **832**, 171
- Turner M. L., Schaye J., Steidel C. C., Rudie G. C., Strom A. L., 2014, *MNRAS*, **445**, 794
- Upton Sanderbeck P., Iršič V., McQuinn M., Meiksin A., 2019, *MNRAS*, **485**, 5059

- Verhamme A., Schaerer D., Atek H., Tapken C., 2008, *A&A*, **491**, 89  
Verhamme A., et al., 2018, *MNRAS*, **478**, L60  
Wakker B. P., Hernandez A. K., French D. M., Kim T.-S., Oppenheimer B. D., Savage B. D., 2015, *ApJ*, **814**, 40  
Werk J. K., et al., 2014, *ApJ*, **792**, 8  
Wise J. H., Demchenko V. G., Halicek M. T., Norman M. L., Turk M. J., Abel T., Smith B. D., 2014, *MNRAS*, **442**, 2560  
Wotta C. B., Lehner N., Howk J. C., O'Meara J. M., Prochaska J. X., 2016, *ApJ*, **831**, 95

**APPENDIX A: SOURCES IDENTIFIED IN PREVIOUS STUDIES IN THE FIELD OF VIEW.**

This paper has been typeset from a  $\text{\TeX/L\AA\TeX}$  file prepared by the author.

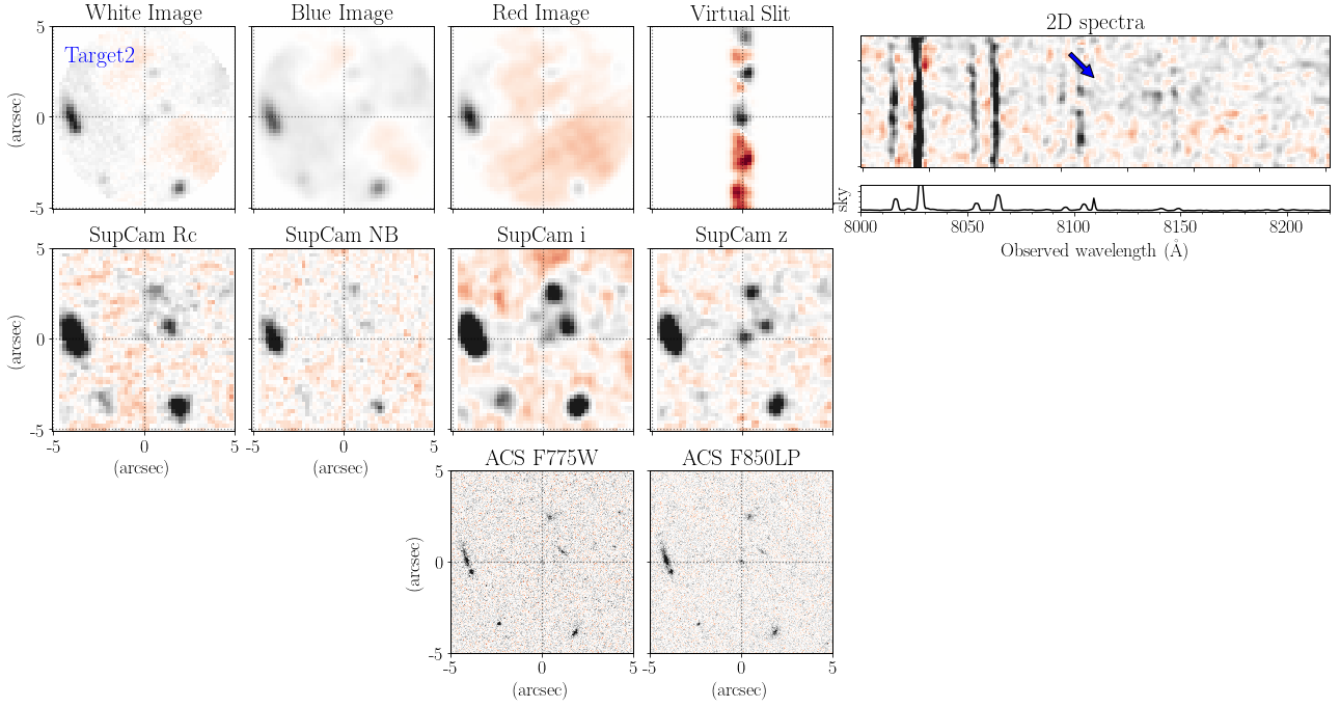


**Figure A1.** Target 2 from [Díaz et al. \(2011\)](#). **Top row:** MUSE thumbnails of  $10 \times 10''$  centered on the object. Blue and Red are broad-band images of  $1000 \text{ km s}^{-1}$  bandwidth at wavelengths bluer and redder than rest-frame  $\text{Ly}\alpha$ . The virtual slit used for the extraction of the 2D spectra is shown using a narrow band image for  $\text{Ly}\alpha$  at  $z_{em} = 5.676$ . The 2D spectrum shows no evidence of emission line. **Middle row:** SuprimeCam images from [Díaz et al. \(2014\)](#). **Bottom row:** ACS HST images in  $i$ -band (F775W) and  $z$ -band (F850LP) from which the object was originally identified ([Stiavelli et al. 2005](#)).

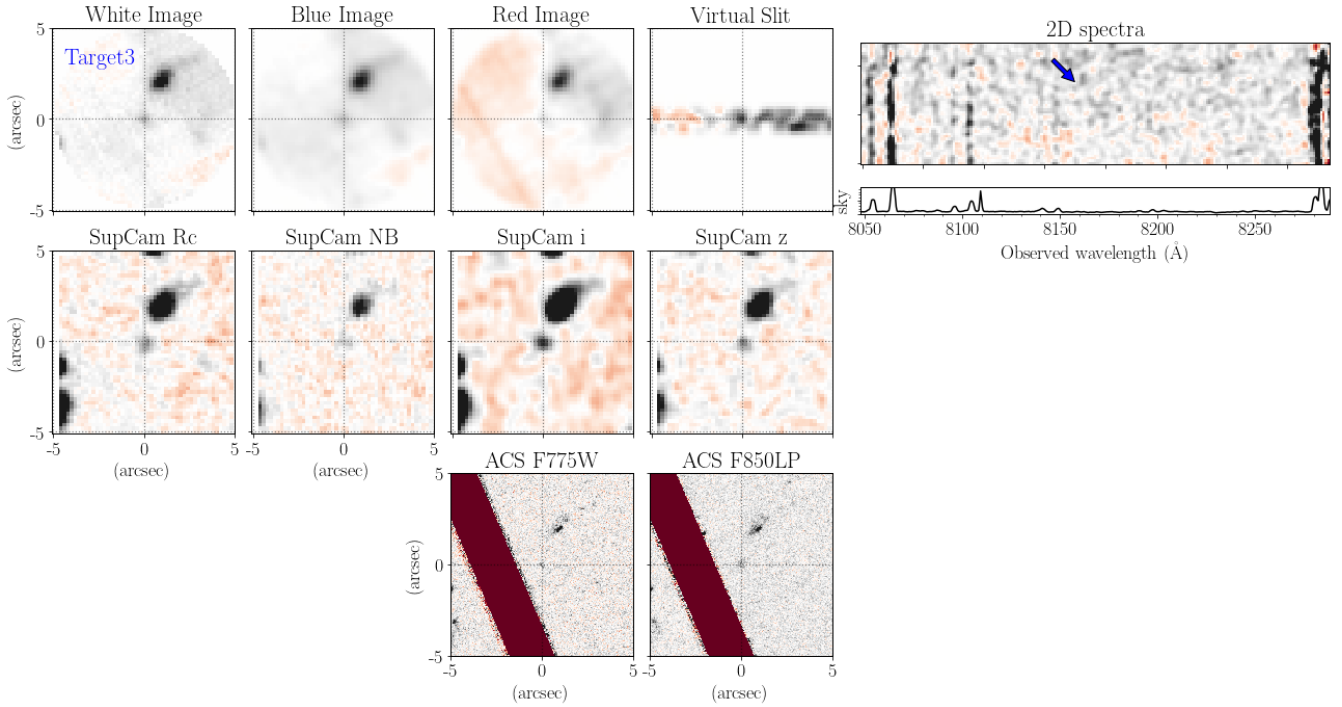


**Figure A2.** Target 3 from [Díaz et al. \(2011\)](#). Description as per Figure A1.

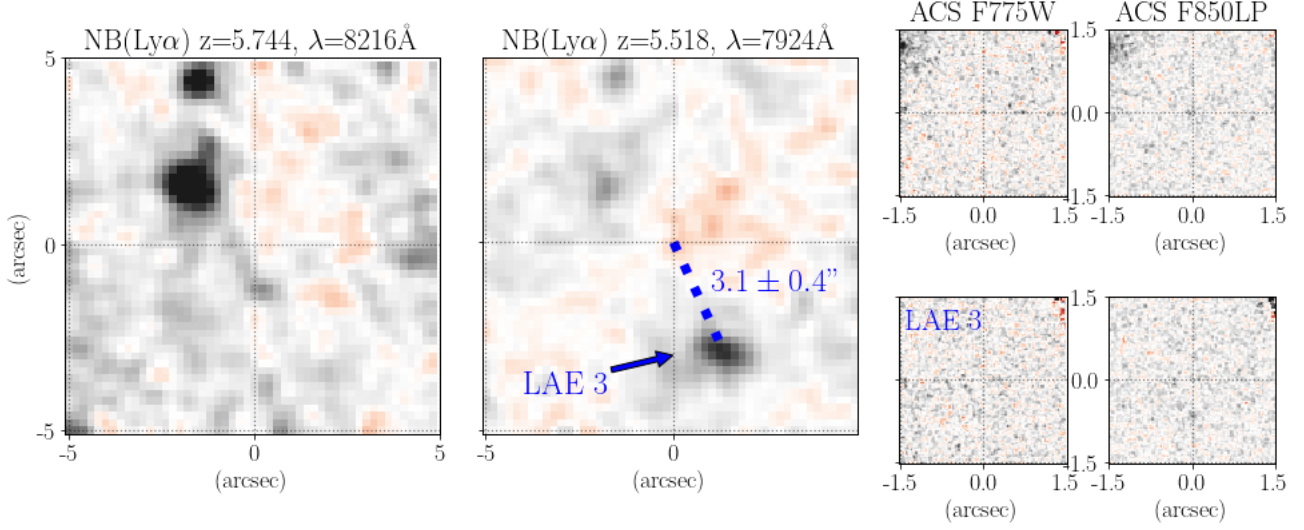


**Figure A3.** Object 1 from Cai et al. (2017). **Left and center:** MUSE thumbnails of  $10 \times 10''$  narrow band images for rest-frame Ly $\alpha$  at  $z_{em} = 5.744$  and  $z_{em} = 5.518$  centered on the object's coordinates. **Right:** ACS HST images in  $i'$ -band (F775W) and  $z'$ -band (F850LP) at the position of Object 1 from Cai et al. (2017) (top) and LAE #3.

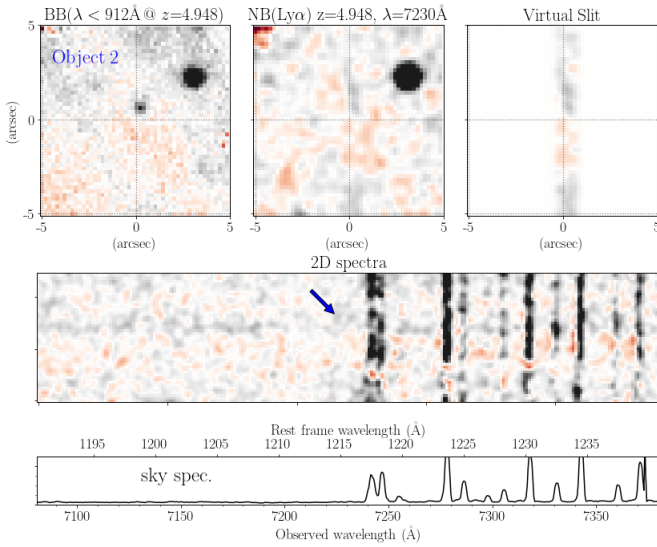


**Figure A4.** Object 2 from Cai et al. (2017). **Top row:** MUSE thumbnails of  $10 \times 10''$  centered on the object. **Left:** BB is a broad-band image including the all wavelengths bluer than rest-frame  $\lambda = 912\text{\AA}$  at  $z = 4.948$ . This image reveals a foreground object slightly above the center of the field. **Center:** Narrow band image for Ly $\alpha$  at  $z_{em} = 5.948$ . No signal is detected. **Right:** Virtual slit used for the extraction of the 2D spectrum. **Middle row:** The 2D spectrum shows no evidence of emission line. However, the continuum of the foreground object is detected across the wavelength range of the image.